nature biomedical engineering

Article

https://doi.org/10.1038/s41551-023-01060-y

Simultaneous quantitative imaging of two PET radiotracers via the detection of positron–electron annihilation and prompt gamma emissions

Received: 15 July 2022

Accepted: 23 May 2023

Published online: 03 July 2023

Check for updates

Edwin C. Pratt[1,2,3], Alejandro Lopez-Montes[4,5], Alessia Volpe[3], Michael J. Crowley[6], Lukas M. Carter[3], Vivek Mittal[6,7,8,9], Nagavarakishore Pillarsetty[3], Vladimir Ponomarev[2,3], Jose M. Udías[4,10], Jan Grimm[1,2,3] ✉ & Joaquin L. Herraiz[4,10] ✉

In conventional positron emission tomography (PET), only one radiotracer can be imaged at a time, because all PET isotopes produce the same two 511 keV annihilation photons. Here we describe an image reconstruction method for the simultaneous in vivo imaging of two PET tracers and thereby the independent quantification of two molecular signals. This method of multiplexed PET imaging leverages the 350–700 keV range to maximize the capture of 511 keV annihilation photons and prompt γ-ray emission in the same energy window, hence eliminating the need for energy discrimination during reconstruction or for signal separation beforehand. We used multiplexed PET to track, in mice with subcutaneous tumours, the biodistributions of intravenously injected [^{124}I]I-trametinib and 2-deoxy-2-[^{18}F]fluoro-D-glucose, [^{124}I]I-trametinib and its nanoparticle carrier [^{89}Zr]Zr-ferumoxytol, and the prostate-specific membrane antigen (PSMA) and infused PSMA-targeted chimaeric antigen receptor T cells after the systemic administration of [^{68}Ga]Ga-PSMA-11 and [^{124}I]I. Multiplexed PET provides more information depth, gives new uses to prompt γ-ray-emitting isotopes, reduces radiation burden by omitting the need for an additional computed-tomography scan and can be implemented on preclinical and clinical systems without any modifications in hardware or image acquisition software.

Positron emission tomography (PET) in combination with computed tomography (CT) is a gold-standard imaging technology in both clinical and preclinical molecular imaging. The traditional workhorse radiotracer, 2-deoxy-2-[^{18}F]fluoro-D-glucose ([^{18}F]FDG or ^{18}FDG), is used in PET/CT mostly for identifying metabolically active cancers[1], although uptake could also result from inflammation, infection or physiologic uptake. Research in molecular imaging has led to a wide range of radiotracers targeting disease-specific cellular markers. Molecular

[1]Department of Pharmacology, Weill Cornell Graduate School, New York, NY, USA. [2]Molecular Pharmacology, Memorial Sloan Kettering Cancer Center, New York, NY, USA. [3]Department of Radiology, Memorial Sloan Kettering Cancer Center, New York, NY, USA. [4]Nuclear Physics Group, EMFTEL and IPARCOS, Complutense University of Madrid, Madrid, Spain. [5]Department of Biomedical Engineering, Johns Hopkins University, Baltimore, MD, USA. [6]Department of Cell and Developmental Biology, Weill Cornell Graduate School, New York, NY, USA. [7]Department of Cardiothoracic Surgery, Weill Cornell Medicine, New York, USA. [8]Neuberger Berman Lung Cancer Center, Weill Cornell Medicine, New York, USA. [9]Sandra and Edward Meyer Cancer Center, Weill Cornell Medicine, New York, USA. [10]Instituto de Investigación Sanitaria Hospital Clínico San Carlos, Madrid, Spain. ✉e-mail: grimmj@mskcc.org; jlopezhe@ucm.es

medicine is now sequencing entire tumour genomes for most patients. However, PET imaging remains a monochromal modality, using one radiotracer per imaging session. Sequential PET scans to detect additional signatures with other tracers could be scheduled, but this is costly and dependent on several factors, such as the sufficient decay of one tracer over time[2] and patient compliance. Repeated imaging also increases radiation exposure from each accompanying CT scan, which can be as high as twice that of a single PET scan[3]. Furthermore, sequential PET scans have a temporal lag time between the two recorded parameters, decreasing biological continuity as well as patient convenience and compliance[2]. Alternatively, blood samples lack the spatial information of PET imaging. Many markers, such as immune cells, reside in the tissues and not in the blood, implying that blood samples can provide only little information about the actual events in tissues[4]. Here multiplexed PET (mPET) expands radiotracer-derived information density during a PET/CT scan, allowing for the synchronization of two compatible radiotracers from known imaging workflows to the same scan session, provided that the isotope pair is mPET compatible.

Multiplexed imaging[5,6] broadly applies different imaging modalities[7], fluorescent emissions[8,9] or γ-rays in the case of single-photon emission computed tomography[10] (SPECT) to identify each distribution. Previous PET multiplexing methods have used specialized sequential scanning with short-lived isotopes[11], compartmental modelling from previous single-tracer scans[12], multiple list-mode reconstruction[13] or a preferential decay of one isotope over another. Sequential scanning increases the gap time required for the decay of one tracer before being able to image the other and also increases the dose from the repeated CT scans. The main disadvantage of compartment modelling is the requirement of information from previous single scans, yielding a method that is radiotracer specific and organ specific. Improvements in PET acquisition and reconstruction technology have included exceedingly fast processing by graphics processing unit (GPU) systems[14] as well as corrections for highly energetic positrons[15,16]. Many PET isotopes have additional γ-rays that require further corrections[17], including background compensation[18,19], patient-specific corrections[20] and geometric scatter corrections for three-dimensional (3D) reconstruction[21]. New deep-learning[22] and whole-body tracking methodologies[23] are further reducing the PET dosage required. Despite the wealth of possible corrections and dose improvements, PET remains a single radiotracer system using mostly ^{11}C or ^{18}F.

Once a positron (β^+) is emitted, it rapidly annihilates with an electron, yielding two 511 keV γ-rays in opposite directions, where they can be detected in coincidence (~3.5 ns) in a detector ring surrounding the object. Between the two detectors that identified the coincidence, a virtual line connects the coincidence; this is known as the line of response (LOR) with the probable origin of the positron on that line. These LORs can be summed into a sinogram, and then reconstructed into a tomographic image. Current PET scanners are designed to detect and record these coincidences (doubles) from purely β^+-emitting isotopes (Table 1). However, when $\beta^+\gamma$ emitting isotopes are used (Table 2), the prompt γ-rays emitted per decay can be detected together with the doubles giving rise to triples, or even multiple coincidences[24,25]. The relative abundance of these events mostly depends on the decay scheme of the isotope (number of prompt γ-rays emitted per positron emission and their energy), the energy of the γ-rays and the sensitivity of the scanner[24]. Most PET scanners store triples in the list-mode data as a set of contiguous double coincidences. These double coincidences are not reconstructed, as they provide two incorrect origins of the radioisotope, reducing the perceived quality of the reconstructed image from these isotopes[17,20,26,27] with the solution often to reduce the detector energy window to omit the prompt gamma or to use another isotope entirely. It is important to note that mPET needs the combination of a prompt gamma and a pure emitting positron for the separation to occur and that the prompt gamma can be detected on the scanner and has a relatively high prompt emission rate to that of the positron (Table 2). mPET leverages the prompt gamma emission as the identifier for the second isotope (as a 'tag'), without requiring any energy discrimination during reconstruction.

Table 1 | Positron emitting isotopes

Doubles	Half-life	β^+ yield (%)
^{15}O	2.04 min	100
^{13}N	9.96 min	100
^{11}C	20.36 min	100
^{68}Ga	68 min	89
^{18}F	109.7 min	97
^{64}Cu	12.7 h	17.6
^{89}Zr	3.3 days	23

Table 2 | Prompt γ-emitting isotopes

Triples	Half-life	β^+ yield (%)	Main prompt γ (keV) and (β^+ γ/β^+ yield)
^{82}Rb	1.27 min	95	777 (13%)
^{52m}Mn	21.1 min	97	1,434 (96%)
^{60}Cu	23.7 min	93	1,333 (88%)
^{94m}Tc	52.0 min	70	871 (96%)
^{110m}In	1.15 h	62	658 (99%)
^{120}I	1.35 h	46	560 (72%)
^{44}Sc	3.97 h	94	1,157 (100%)
^{86}Y	14.7 h	33	1,080 (83%), 627 (33%)
^{76}Br	16.2 h	26	559 (58%)
^{72}As	1.08 days	88	834 (79%)
^{124}I	4.18 days	23	602 (51%)
^{52}Mn	5.59 days	29	744 (19%), 1,434 (100%)

Results and discussion

Here we propose a general method[25] for separating and reconstructing double coincidences from triple coincidences (Fig. 1) by implementing an additional independent reconstruction method (Supplementary Fig. 1a) solely for list-mode double coincidences, generating two separate datasets for each PET scan (Fig. 2 and Supplementary Fig. 1b,c). These datasets can be refined with iterative reconstructions using the abundance ratios from previous cylinder sensitivity and uniformity phantom studies (Supplementary Fig. 1d) to produce quantitative[28] mPET images (Supplementary Fig. 1e,f) with similar reconstruction performance to traditional LOR reconstruction methods with sufficient iterations (Supplementary Fig. 1g,h) at a total reconstruction time around 30 min on a central processing unit (CPU) for a two-isotope method without subsets or approximations (see Methods). Because many PET scanners do not record the energy associated with the individual event, the detected prompt γ-ray triple is differentiated instead by the type of LOR used for the reconstruction. Reconstruction and correction methods for standard PET are focused on coincidences using a single LOR. When three coincident γ-rays are detected, three LORs are possible; however, predominantly only two LORs are detected and stored as double coincidences in the list mode. In this reconstruction approach, the two LORs previously omitted from a triple coincidence can be combined as a V-shaped LOR (VLOR), better approximating the origin of the radioisotope (Supplementary Fig. 1a). VLOR reconstruction has been widely implemented in multiplexed pinhole SPECT

https://doi.org/10.1038/s41551-023-01060-y

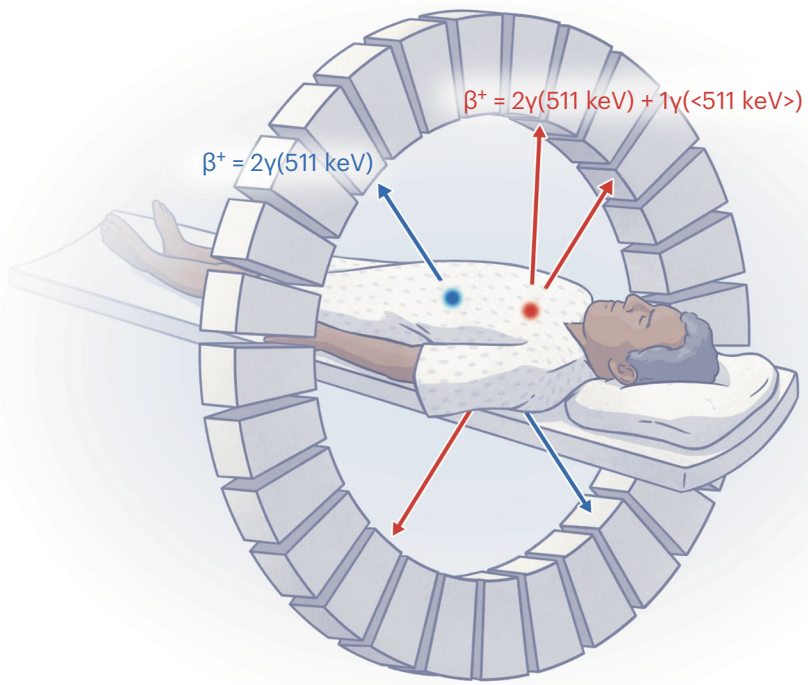

Fig. 1 | Overview of mPET using a pure positron and positron–gamma radionuclide pair. PET uses 511 keV annihilation photons from an emitted positron for imaging, recording the pair of photons as a coincident event called a 'double' (blue β⁺). Other positron-producing radionuclides can emit a positron and an additional gamma particle detected within the traditional coincidence-timing window, called a 'triple' (red β⁺). Traditionally, triple events are considered spurious and not reconstructed, and energy windows of triple-emitting radionuclides often are adjusted to limit triple events. By increasing the coincidence energy window to include the prompt gamma while also providing a reconstruction method for triple coincidences, two-isotope distribution can be reconstructed from the list-mode events via mPET. This method can reconstruct both isotopes solely on how events are recorded: as double-coincidence or triple-coincidence events. For detectors with sufficient energy resolution that register energy with event coincidence, additional isotope parings could be further multiplexed with each unique prompt gamma energy.

imaging[29] and has yet to be used as part of PET reconstruction. Thus, acquiring list-mode PET scans containing both double-emitting and triple-emitting radioisotope and reconstructing triple coincidences as VLORs allows two PET isotopes to be effectively separated simply on the basis of the type of coincidence recorded and without the need for energy discrimination of the γ-rays in reconstruction. To the best of our knowledge, this is currently not possible on standard commercial PET scanners. Therefore, this method represents a fundamental advancement over previous proposed methods[13,30–32] and opens most preclinical and clinical PET scanners to the simultaneous acquisition of two rationally paired radiotracers.

The maximum-likelihood expectation–maximization (MLEM) reconstruction of VLORs in list mode corresponds to the standard expression for iterative reconstruction of VLORs (equation (1)):

$$x_j^{n+1} = x_j^n \frac{\sum_v a_{vj}\left(\frac{1}{P_v}\right)}{s_j} \quad (1)$$

where x_j^n is the value of voxel j on the current reconstruction at iteration n, s_j represents the sensitivity of voxel j, and a_{vj} is the probability that an emission at voxel j is detected at VLOR v. As each VLOR v consists of two joined LORs, the projection in a VLOR P_v can be simply estimated as the sum of the projections in each of the two LORs ($P_v = P_{v1} + P_{v2}$). VLOR reconstruction can be considered similar to standard reconstruction but with two-times larger LORs. If reconstruction with sinograms is preferred, it can be obtained from VLOR data using the following procedure: (1) define the relative contribution or weight w_{v_i} of each LOR to the VLOR as $w_{v_1} \equiv P_{v_1}/(P_{v_1} + P_{v_2})$ and $w_{v_2} \equiv P_{v_2}/(P_{v_1} + P_{v_2})$. In the initial iteration, $w_{v_1} = w_{v_2} = 0.5$; (2) rewrite the numerator in the MLEM expression as

$$\sum_v a_{vj}\left(\frac{1}{P_v}\right) = \sum_v a_{vj}\left(\frac{1}{P_{v1}+P_{v2}}\right) = \sum_{v_1} a_{v_1 j}\left(\frac{w_{v_1}}{P_{v_1}}\right) + \sum_{v_2} a_{v_2 j}\left(\frac{w_{v_2}}{P_{v_2}}\right) = \sum_{v_i} a_{v_i j}\left(\frac{w_{v_i}}{P_{v_i}}\right)$$

where i is the LOR index. Therefore, one can work with the individual LORs from the VLORs just by using the weights w_{v_i} (instead of '1', as it is done in standard list-mode PET) that correspond to the relative value of their projections; (3) use the weights of each LOR from the VLOR. The weighted data are stored in a standard sinogram, and the sinogram is updated before each new iteration, following these three steps.

Taken together, we show that the mPET reconstruction method can be applied to data acquired in list-mode format in commercially available preclinical and clinical PET/CT systems. We demonstrate first in phantoms the principle and quantitative capacity of mPET separation. Next, we show several examples using previously published and validated targets to highlight the possibilities that simultaneous PET isotope imaging may offer. We demonstrate in several animal therapy models the ability of mPET to easily identify two radiolabelled small-molecule radiotracers, [^{124}I]I-trametinib and [^{18}F]FDG. We also use mPET for the evaluation of nanoparticle-mediated drug delivery with [^{124}I]I-trametinib loaded passively onto [^{89}Zr]Zr-ferumoxytol (a clinically used iron oxide nanoparticle capable of carrying select small molecules in its coating[33]). Lastly, prostate-specific membrane antigen (PSMA)-targeted chimaeric antigen receptor (CAR) T-cells were engineered to express the sodium iodide symporter (NIS) to render them

https://doi.org/10.1038/s41551-023-01060-y

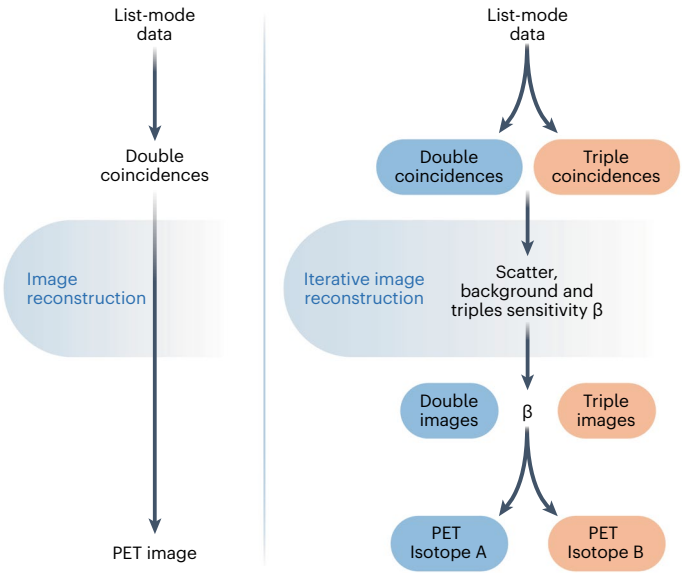

Fig. 2 | mPET processing workflow in comparison with traditional PET. Left: traditional PET image workflow processes coincident events for normalization, sinogram formation and 2D or 3D reconstruction. Right: mPET image processing expands the reconstruction to account for traditional coincidences and triple coincidences, as well as for the proportion of random prompts to both categories. This iteration is isotope specific and system specific, including factors such as scatter within the detector field of view (see Methods for processing details). Machine and isotope factors can be determined a priori with uniformity and mixture phantoms.

traceable in vivo by PET[34]. We used mPET to simultaneously visualize the distribution of NIS-expressing CAR T-cells to the PSMA-expressing tumours by ^{124}I and ^{68}Ga-PSMA-11 PET, respectively. mPET is an image reconstruction method that enables true mPET imaging from standard PET scanners without the need of any hardware or acquisition-software modification through a general PET reconstruction method.

Imaging of phantoms

To test the feasibility of the mPET method on a preclinical scanner, phantom experiments were performed on a PET/CT system capable of acquiring list-mode data. Capable PET/CT systems include the preclinical Inveon PET/CT (Siemens Medical Solutions, which we used) and the SuperArgus (Sedecal), as well as the clinical Biograph MCT PET/CT (Siemens Medical Solutions), among other potential list-mode acquisition scanners. To set up the system for mPET acquisition, a new PET protocol was configured by expanding the upper energy range from 650 keV to 700 keV to maximize the capture of the 511 keV annihilation photons and the prompt gamma in the same energy window. The full energy range of was not selected, to reduce random event noise and multiple coincidences from Iodine-124 (^{124}I). As PET detectors possess energy resolutions on the order of 20% of the energy of the photopeak, additional energy range is necessary beyond the 511 keV and prompt gamma to capture the majority of emitted photopeaks[7]. Cylindric uniformity and sensitivity phantoms containing 1 l with 9.25 MBq (250 µCi) of each isotope separately were acquired with the new energy settings to determine detector uniformity and used to estimate the double-to-triple sensitivity ratio (Supplementary Fig. 2a). These phantom calibrations are specific to the isotope mixture and scanner used and can be applied after mPET image acquisition. To test the separation performance of mPET, a hollow body (for background activity) and four distinct cavities were prepared containing different mixtures of two isotopes, Zirconium-89 (^{89}Zr) and ^{124}I. ^{89}Zr is considered a double-emitting isotope, whereas ^{124}I is a triple-emitting isotope (Table 1). Despite the prominent emission of the additional 909 keV photopeak by ^{89}Zr, this emission is not within the coincident timing window (3.6 ns) and is thus only viewed by a PET detector as a double-emitting isotope. The phantom as mixed was acquired with a 350–700 keV energy window for 30 min. The subsequently acquired list-mode file was processed using the standard histogram and two dimensional (2D) ordered subset expectation maximization (OSEM2D) reconstruction algorithm as well as independently with the mPET reconstruction method. As seen in Fig. 3a, processing with the traditional PET OSEM2D reconstruction method yields a phantom cavity as well as cavities 1 to 4 with a uniform distribution in the cavity, yet a reduced signal of ^{124}I as many events are discarded as scatter (triples) and not reconstructed. Using the mPET reconstruction method, we observed the separation of both ^{89}Zr (Fig. 3b) and ^{124}I (Fig. 3c) in the phantom cavities and show that separation was possible on a preclinical PET/CT scanner. In Fig. 3d the activity measured with mPET in each cavity agreed with previous activities measured during phantom preparation, confirming the accuracy of the measurement and separation.

We further tested the performance of mPET reconstruction by using a mouse bearing ^{124}I in the thyroid and obtained similar images with a standard reconstruction as well as mPET (Supplementary Fig. 2b). Furthermore, the activity concentration and pixel position across the mouse thyroid could identically differentiate thyroid lobes with mPET as with the standard reconstruction (Supplementary Fig. 2c). The mPET reconstruction produces similar images to the standard reconstruction, even with multiple subjects present in the scanner (Supplementary Fig. 2d). Additional testing of the linearity of the mPET reconstruction method was done with increasing phantom wells for ^{124}I, in the range of 3.7–44 MBq (100–1,200 µCi), and produced identical images for the standard reconstruction (Supplementary Fig. 3a), doubles by mPET (Supplementary Fig. 3b) and triples (Supplementary Fig. 3c) by mPET, where the ratio of triples to doubles did not deviate across the scanner range (Supplementary Fig. 3d). The sensitivity and noise of the mPET method was tested as a function of total counts, with decreasing fractions of the total counts acquired, with 10% of the total counts producing similar images than full counts yet with increased noise (Supplementary Fig. 4a). A change in activity reconstructed was only observed below 20% of the total counts, as the number of triples approached that of the random triples observed in the scanner (Supplementary Fig. 3b). Overall, mPET provided increased image information density with little bias (<10%), similar spatial resolution and contrast and a small relative noise increase (<10%) compared with that obtained with single-tracer PET acquisitions (Supplementary Figs. 2–4).

To test the effectiveness of our method in a clinical scanner, a Siemens Biograph mCT scanner was used to record mPET images of a 3D-printed liver containing a background of ~22 MBq (~600 µCi) ^{89}Zr, while a focal 'liver lesion' was filled with ~20 MBq (~550 µCi) ^{124}I. Traditional PET reconstruction (Fig. 3e) yielded a 'liver' containing a diffuse amount of ^{89}Zr with a hotspot ^{124}I 'lesion'. Upon separation and reconstruction, the 'liver' (Fig. 3f) and 'lesion' (Fig. 3g) signals could be easily differentiated in each channel, where the mPET reconstruction method could be applied to clinical scanning systems and workflows in addition to preclinical systems. We found that both preclinical and clinical systems could acquire data suitable for mPET separation, with preclinical performance nearly identical to that of the standard reconstruction methods, while providing two simultaneous isotope images. With mPET configured on both preclinical and clinical systems, we next prepared several preclinical in vivo experiments with mPET to address a series of biological questions.

Imaging two tumour markers with mPET

Molecular imaging has benefited the development of radiotracers as analogues to clinically approved drugs. The success of [^{18}F]FDG as a molecular imaging tool in oncology exploits the Warburg effect, using the high GLUT1 activity to bring the radiotracer into a glycolytically

https://doi.org/10.1038/s41551-023-01060-y

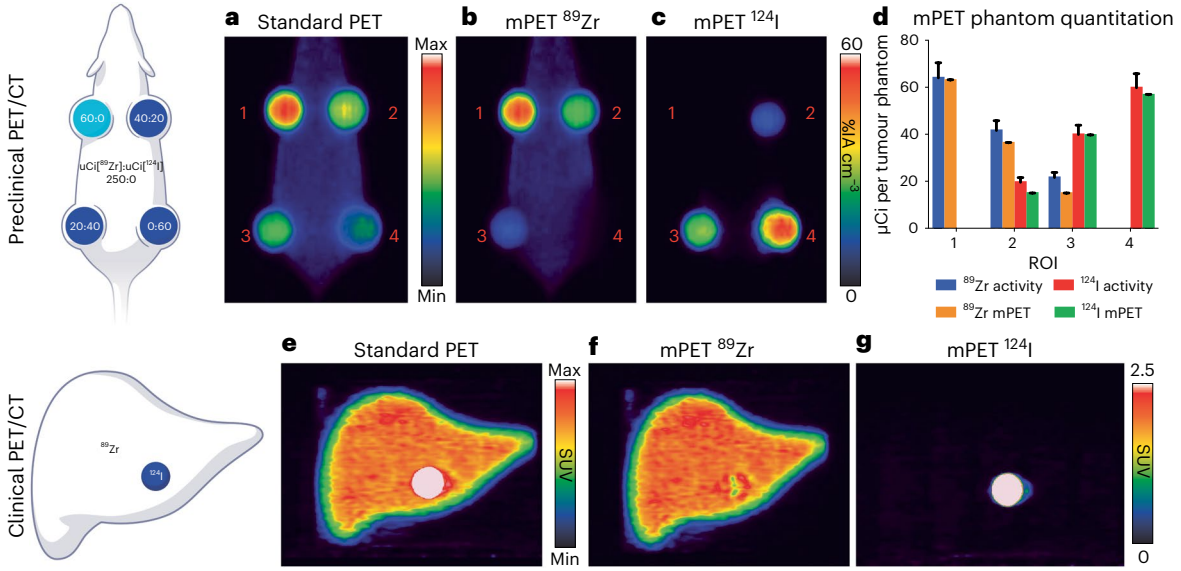

Fig. 3 | Phantom performance of mPET on preclinical and clinical PET/CT systems. a, A phantom containing 9.25 MBq (250 µCi) ^{89}Zr in the cavity with an additional mixture of 2.22 MBq (60 µCi) ^{89}Zr and/or ^{124}I in four exterior cavities was measured on a Siemens Inveon preclinical PET/CT. PET image as acquired using the 350–700 keV energy window and reconstructed with the traditional OSEM2D method, which attenuates the ^{124}I signal partially as scatter, as seen by the reduced intensity in cavity 4. **b**, mPET separation and reconstruction of ^{89}Zr coincidences recapitulates the traditional PET image seen in Fig. 2a without ^{124}I coincidence events. **c**, Using triple coincidences from the list mode, mPET recovered the ^{124}I titration in the phantom. Differences in image quality for the cavities in **a** and **b** result from the lower number of triple events available for reconstruction in **a**, as well as from the increased positron flight of ^{124}I compared with that of ^{89}Zr. **d**, Quantitative recovery of counts in each of the four cavities matches the activity measured during the preparation of the phantom, which shows that the reconstruction method can support the quantitation of two radiotracers simultaneously. **e**, A human-scale liver phantom with 21.8 MBq (590 µCi) ^{89}Zr dispersed in the 1.4 l liver, with a separated 6.5 ml spherical cavity containing 20.7 MBq (560 µCi) ^{124}I. PET image as acquired using the 350–700 keV energy window on a clinical Siemens Biograph mCT clinical PET CT and reconstructed with the traditional OSEM2D method. **f**, mPET separation of ^{89}Zr coincidences residing in the liver phantom, with slightly less signal where the spherical cavity phantom was located. **g**, mPET reconstruction of ^{124}I triple coincidences in the tumour sphere located on top of the liver. Results from a single preclinical or clinical phantom. Values reported in **d** represent mean µCi in each spherical cavity measured from voxel intensities inside the 1 ml cavity ROI. Error bars in **d** represent a Capintec dose calibrator error of 5% from single-activity measurements before addition to the phantom, and the error bars for mPET represent the s.d. of all of the voxel intensities in the ROI. %IA cm^{-3}, percentage of injected activity per cubic centimetre; SUV, standard uptake value.

active cell where it is entrapped[1]. However, not all tumours are highly metabolically active, requiring additional molecular imaging agents for identification and staging. [^{124}I]I-trametinib is an imaging isotopologue of the inhibitor trametinib binding in an allosteric pocket to the MAPK/ERK protein MEK1/2 (ref. 35), targeting proliferating tissue and distinct from [^{18}F]FDG targeting glycolytic activity. With traditional PET imaging, the combination of [^{124}I]I-trametinib with [^{18}F]FDG traditionally would require different imaging sessions owing to isotope-decay overlap. Here mPET reconstruction can bring both imaging agents together to simultaneously determine the GLUT1 and MEK1/2 targeting in melanoma tumours undergoing therapy. [^{18}F]FDG was administered intravenously and imaged 1 h post injection with a previous injection of [^{124}I]I-trametinib 24 h before. Upon separating the doubles ([^{18}F]FDG, bottom row) from the triples ([^{124}I]I-trametinib, top row), two distinct biodistributions were observed (Fig. 4a). [^{124}I]I-trametinib uptake in untreated mice (left column) was seen in the gastrointestinal (GI) tract as well as in the right-flank B16F10 tumour. Mice receiving cold trametinib before radiotracer injection (Fig. 4b) saw blocking in the abdomen and tumour, whereas treatment with vemurafenib targeting the B-Raf protein upstream of MEK (Fig. 4c) yielded a partial reduction in [^{124}I]I-trametinib uptake in the tumour and GI tract. Combination therapy with both cold trametinib and vemurafenib (Fig. 4d) yielded a combination of [^{124}I]I-trametinib uptake from both the vemurafenib and trametinib treatment arms, with low uptake in the tumour and with some clearance in the GI tract. As melanomas are known to be [^{18}F]FDG-avid, high tumour uptake was seen in all mice across treatment groups (Supplementary Fig. 5) alongside the heart, retina, bladder and brain. Quantitative ROI analysis of the tumours treated with trametinib show increased [^{18}F]FDG uptake compared with untreated tumours and with tumours treated with vemurafenib and trametinib (Supplementary Fig. 5f), with axial slices of the mice shown in Fig. 4 (Supplementary Fig. 6). The increase in [^{18}F]FDG uptake occurs when BRAF wildtype tumours are given BRAF/MEK inhibitor, leading to an increase in GLUT1 expression[36] (although this study only showed MEK inhibition). Additional mPET images of other mice in each arm can be found in Supplementary Fig. 5 and highlight the versatility and the unbiased separation of the reconstruction method. Overall, we found that dual small-molecule drug imaging with mPET could be used to track tumour inhibition of MEK during therapy while also maintaining a standard PET [^{18}F]FDG image for glycolytic activity, providing deeper insight into tumour metabolism in situ.

Imaging a drug and nanoparticle carrier with mPET

Nanoparticles have been widely used as formulation enhancers, carrying insoluble drugs but also as agents to alter drug biodistribution, ideally lowering off-target delivery and its associated side effects. Examples are Doxil, nab-paclitaxel and most recently mRNA delivery for SARS-CoV2 vaccination[37]. Many studies rely on tracking just one component of the drug-loaded nanoparticle to assess delivery, usually the radiolabelled nanoparticle, and assume that the distribution of the drug in the nanoparticle is analogous to the distribution of the nanoparticle. With mPET, both a radiolabeled drug and nanoparticle can be noninvasively monitored and quantified. Ferumoxytol, an iron oxide nanoparticle approved by the US Food and Drug Administration for anaemia, can be loaded with various small-molecule cargo into its

https://doi.org/10.1038/s41551-023-01060-y

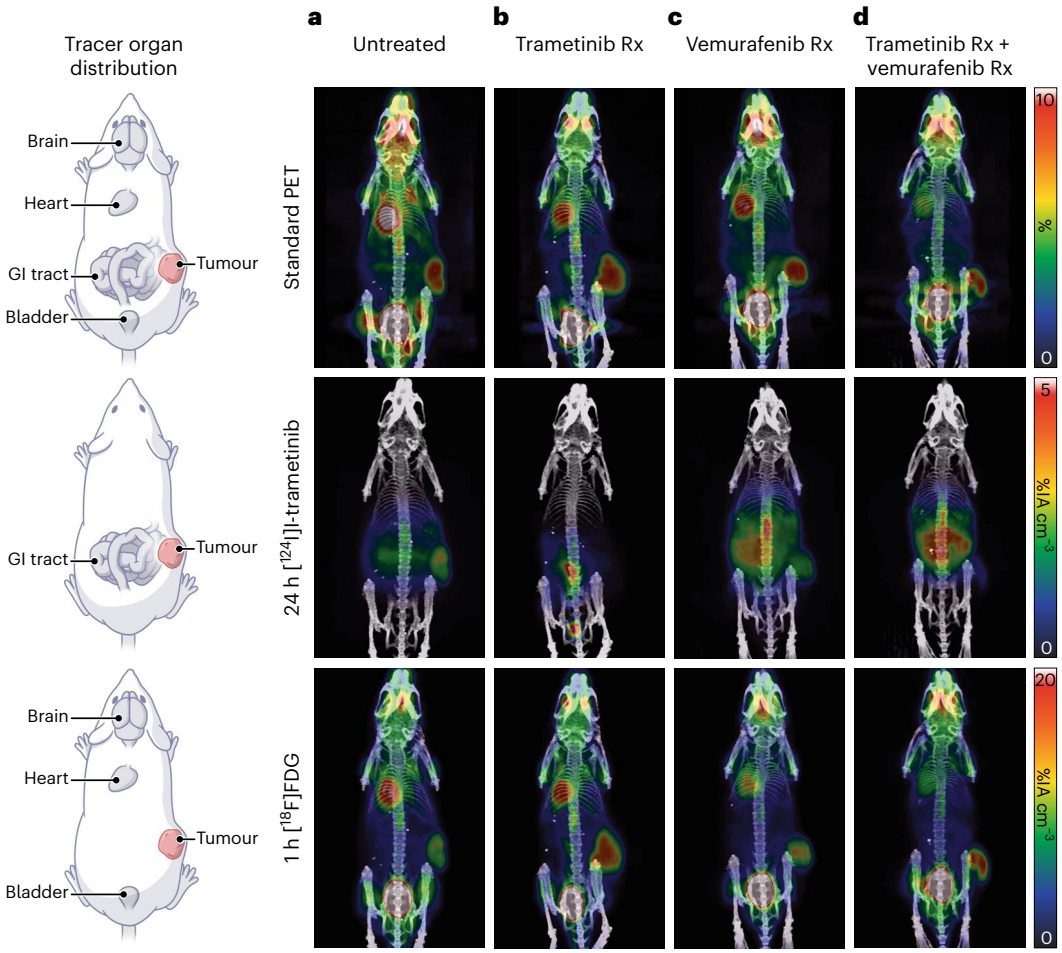

Fig. 4 | mPET of two small-molecule radiotracers for enhanced therapy monitoring. a–**d**, Mice bearing B16F10 melanoma tumours on the right flank were administered ~14.8 MBq (~400 µCi) [^{124}I]I-trametinib and ~7.4 MBq (~200 µCi) [^{18}F]FDG 24 h and 1 h before PET imaging, respectively. mPET reconstruction separated both radiotracers. **a**, [^{124}I]I-trametinib in the tumour with some clearance in the GI tract for an untreated mouse. [^{18}F]FDG was observed in the tumour, bladder, heart and brain. mPET separated the two radiotracers present in the same mouse, quantitating MEK-inhibitor binding and glucose metabolism. **b**,**c**, In mice treated therapeutically with unlabelled nonradioactive trametinib (**b**) or with vemurafenib the [^{124}I]I-trametinib (**c**) uptake was blocked and reduced, respectively, as expected for on-target and upstream MEK inhibition. **d**, Combination therapy of vemurafenib and trametinib showed a blend of [^{124}I]I-trametinib distribution from both individual therapy arms, although tumour uptake was also blocked as expected. By using mPET, the additional [^{18}F]FDG or [^{124}I]I-trametinib information was available for each mouse. Quantitative coronal slices can be found in Supplementary Fig. 6. ROI analysis revealed higher [^{18}F]FDG uptake (Supplementary Fig. 5f) in mice undergoing MEK-inhibitor therapy, compared with untreated, BRAF or BRAF + MEK-treated mice (Supplementary Fig. 5). Here mPET enabled the non-invasive assessment of MEK and GLUT1 under therapy in the individual tumours. $n = 4$ mice per treatment group, $n = 16$ mice in total.

coating[33] and used in lymph-node-mapping studies[38] after delivery to the tumour. Ferumoxytol has been radiolabelled using a chelate-free and heat-induced labelling method, allowing PET imaging of ferumoxytol distribution in vivo[39,40]. For trametinib (Mekinist), although effective, its use in patients is discontinued owing to on-target toxicity in the form of severe rashes and GI distress[41]. Using mPET with [^{89}Zr]Zr-ferumoxytol loaded with [^{124}I]I-trametinib may elucidate the contribution of each component in nanoparticle delivery. We loaded [^{124}I]I-trametinib onto [^{89}Zr]Zr-ferumoxytol using a variety of methods, achieving a loading yield of around 20–30% with a bovine-serum-albumin coating and via co-loading with nonradioactive trametinib (Supplementary Fig. 7), allowing for direct quantitation of [^{124}I]I-trametinib post-loading and purification. [^{124}I]I-trametinib loaded onto [^{89}Zr]Zr-ferumoxytol was then administered into a mouse bearing a B16F10 melanoma on the left dorsal foot pad and imaged at 0.25, 2, 6, 12, 24, 48 and 96 h using mPET. It became clear that soon after injection the [^{124}I]I-trametinib distribution (Fig. 5) did not match that of the carrier nanoparticle [^{89}Zr]Zr-ferumoxytol, meaning that, despite in vitro loading and stability suggesting the contrary, most of the drug had dissociated rapidly from the nanoparticle in vivo. Subsequent imaging timepoints revealed accelerated clearance of [^{124}I]I-trametinib by 24 h and its absence at 96 h (Extended Data Fig. 1). Although passive loading with this drug–nanoparticle combination was unsuccessful in vivo, mPET could separate the signals from the drug and the nanoparticle, allowing for quick confirmation of the instability of the loaded combination, which was not expected and therefore revealing important information. Hence, mPET provides the ability to track both nanoparticle and payload, a process that currently cannot be done with one radiotracer alone in the same PET image and that is often only confirmed with a fluorescent or colorimetric dye acting as a drug surrogate.

Tracking of CAR T-cells and PSMA with mPET

There is increasing focus on immunoPET radiotracers to track immune populations such as T cells, to observe their infiltration or activation during therapy. Engineering of CAR T-cells to target a specific antigen and to include reporter genes represents a versatile imaging

https://doi.org/10.1038/s41551-023-01060-y

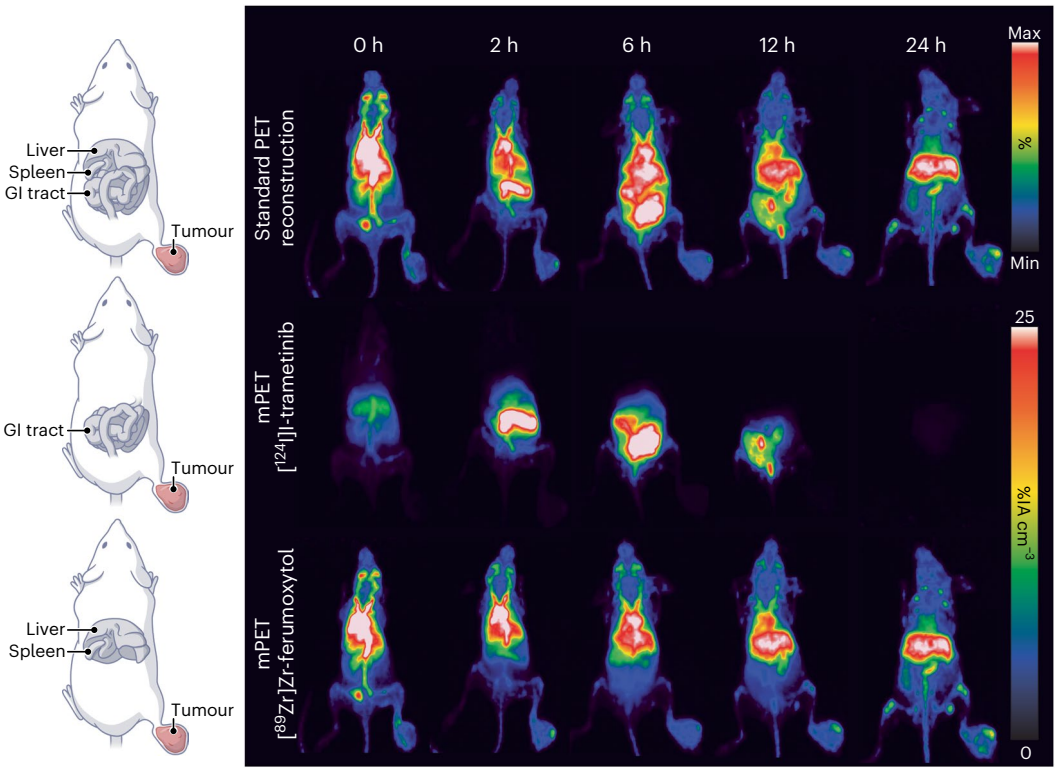

Fig. 5 | Visualizing nanoparticle delivery with mPET. Biodistribution of ~7.4 MBq (~200 µCi) [^{124}I]I-trametinib loaded onto ~9.3 MBq (~250 µCi) ^{89}Zr-ferumoxytol in a mouse bearing a B16F10 melanoma on the right dorsal foot pad through 96 h. Top: traditional PET reconstruction shows distribution over 24 h to mainly the liver and spleen, with some uptake in the dorsal foot pad and popliteal lymph node. Further imaging between 24 h and 96 h shows no noticeable change in biodistribution (Extended Data Fig. 1). Middle and bottom: initial mPET imaging identifies the distinct biodistribution of [^{124}I]I-trametinib and [^{89}Zr]Zr-ferumoxytol, suggesting that [^{124}I]I-trametinib was not retained on the ferumoxytol surface. Middle: [^{124}I]I-trametinib was observed to clear rapidly via hepatobiliary excretion, with no appreciable activity remaining after 24 h. [^{124}I]I-trametinib loading was facilitated with cold trametinib; thus, the release of trametinib could also block the uptake of [^{124}I]I-trametinib in the dorsal foot pad, reducing the delivery of free [^{124}I]I-trametinib to the tumour. Bottom: delivery of only [^{89}Zr]Zr-ferumoxytol to the dorsal foot pad tumour appears to have occurred by mPET. We used one mouse, and $n = 7$ imaging timepoints in mPET.

therapeutic system. We retrovirally transduced human T lymphocytes to express a tricistronic cassette (Extended Data Fig. 2a) comprising the PSMA-targeting second-generation CAR, the human NIS[34] and the membrane-anchored *Cypridina* (maCluc) reporter genes[9], thus enabling non-invasive in vivo therapeutic cell tracking by PET and bioluminescence imaging (BLI), respectively. CAR T-cell anti-tumour activity and reporter function were assessed in vitro (Extended Data Fig. 2a–h and Supplementary Fig. 8), followed by in vivo bilateral tumour measurements post-administration of the CAR T-cells (Extended Data Fig. 2i). Here mPET was used to separate the distribution of CAR T-cells targeting PSMA-positive cells via ^{124}I while simultaneously measuring PSMA-positive tumour location and expression with [^{68}Ga]Ga-PSMA-11. Mice were administered ^{124}I 2 h before and [^{68}Ga]Ga-PSMA-11 1 h before mPET imaging. The mice had a PSMA-positive tumour (left shoulder) with an adjacent PSMA-negative tumour (right shoulder) as a control. With standard reconstruction, uptake was seen in the PSMA-positive tumour along with the organs that endogenously expressed NIS (such as the thyroid, salivary glands and the stomach) and tracer clearance (such as the kidneys and the bladder) (Fig. 6b). The separation of [^{68}Ga]Ga-PSMA-11 and ^{124}I shows that there were distinct distributions of [^{68}Ga]Ga-PSMA-11 in the PSMA-positive tumour, kidneys and bladder (Fig. 6c), whereas ^{124}I was found also in the PSMA-positive tumour, thyroid, kidneys, stomach and bladder (Fig. 6d). Individual axial slices through the PSMA-positive and PSMA-negative tumours show the distribution of ^{68}Ga-PSMA-11 and ^{124}I; both are located in the tumour, although with different intratumoural distributions. BLI of mice before mPET imaging agrees with the CAR T-cell targeting seen by ^{124}I imaging and with PSMA-positive tumour imaging with [^{68}Ga]Ga-PSMA-11. An expanded view containing unseparated and mPET reconstructed images for each mouse in the imaging cohort can be seen in Supplementary Fig. 9a, with overall distribution for each isotope and tumour slices (Supplementary Fig. 9b). A video overlaying [^{68}Ga]Ga-PSMA-11 and ^{124}I clearly shows the difference in distribution at two intensity levels (Supplementary Videos 1 and 2), whereas a geometric mean representation of the image product identified more similarities in radiotracer distribution than in the original separated differences (Supplementary Fig. 10). A bicistronic cassette without NIS was also generated using ^{89}Zr-Oxine for ex vivo CAR T-cell labelling in combination with [^{86}Y]Y-DOTA-PSMA (Extended Data Fig. 3), showing similar PSMA-positive targeting by CAR T-cells. Here the mPET reconstruction provided a method to simultaneously track distribution and targeting of CAR T-cells to PSMA-positive tumours while confirming PSMA expression in vivo during the same PET scan.

Dual immunoPET identifying T-cell exhaustion with mPET

Although CAR T cells and clinically approved peptides or small molecules are of great utility for PET imaging, the use of radiolabelled antibodies for immunoPET can provide exquisite sensitivity and specificity as molecular imaging agents of membrane-bound antigens. These immunoPET agents often require days to circulate for maximal uptake in the tumour, although newer labelling systems such as the inverse electron demand Diels–Alder reaction have decoupled antibody circulation with imaging distribution[42,43] to reduce off-target radiation exposure. As a molecular imaging tool, antibodies or their fragments targeting the immune system and CD8$^+$ T cells[44] have been developed to identify immune infiltration, known as pseudoprogression, in solid

https://doi.org/10.1038/s41551-023-01060-y

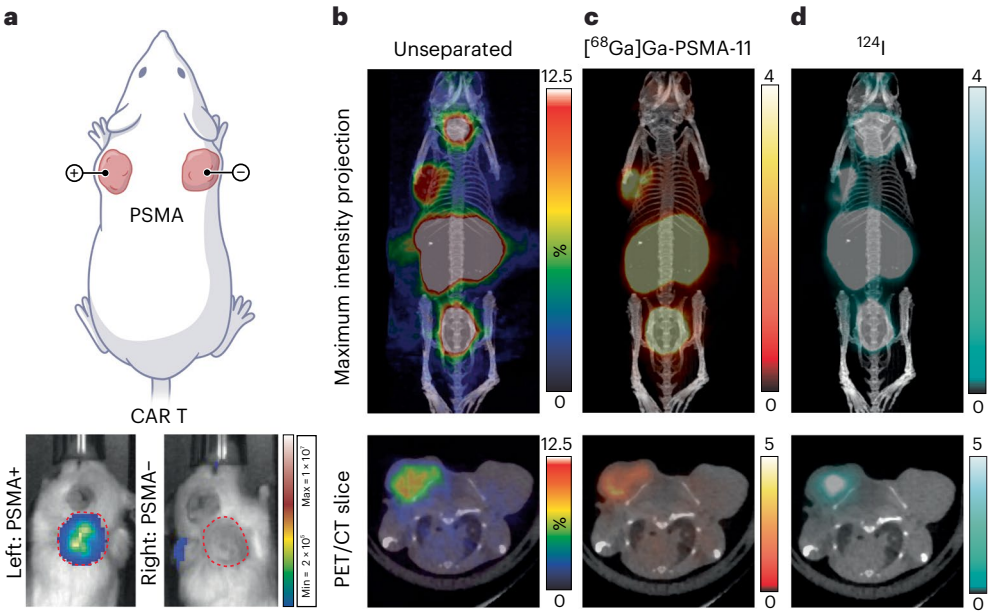

Fig. 6 | Tracking CAR T-cell therapy with mPET. a–d, Mice bearing PSMA-positive (left) and PSMA-negative (right) tumours were administered CAR T-cells bearing a tricistronic construct hNIS.P28z.exCLuc targeting PSMA and expressing the NIS reporter gene (Extended Data Fig. 2 and Supplementary Fig. 8). On day 7 post CAR T-cell administration, BLI was performed to identify PSMA targeting to tumours; subsequently, ~10.4 MBq (~280 µCi) [^{124}I]I was added to identify the NIS-positive cells (that is, the distribution of CAR T-cells). One hour after [^{124}I]I administration, ~13.7 MBq (~370 µCi) [^{68}Ga]Ga-PSMA-11 was administered to identify PSMA-positive tumour tissue, at which point mPET imaging was conducted. Traditional PET imaging (uncalibrated) shows high uptake in the kidneys, bladder and thyroid, owing to the normal distribution and clearance of both [^{124}I]I and [^{68}Ga]Ga-PSMA-11, with uptake in the PSMA-positive tumour. mPET imaging reveals CAR T-cell distribution via [^{124}I]I and PSMA expression within the PSMA-positive tumours. Individual mice and isotope separations can be seen in Supplementary Fig. 9. Furthermore, an orthogonal CAR T-cell mPET experiment using ex-vivo-labelled [^{89}Zr]Zr-oxine CAR T-cells in combination with [^{86}Y]Y-DOTA-PSMA also confirmed targeting to PSMA-positive tumours (Extended Data Fig. 3). We used five mice for tricistronic mPET imaging of CAR T-cells (data from individual mice are shown in Supplementary Fig. 9). We used one representative mouse in Extended Data Fig. 3. BLI radiances are shown in photons per second per square centimetre per steradian.

tumours during PD-1 immunotherapy[45]. Newer targets defining subpopulation and activation states of CD8$^+$ T cells have proposed defining the state of T-cell exhaustion with tumour burden. More recently, the functional differences between progenitor-exhausted and terminally exhausted tumour-infiltrating lymphocytes have been shown to have distinct functional properties, such that under PD1 therapy a high ratio of progenitor-exhausted tumour-infiltrating lymphocytes confers a greater overall survival[46]. Progenitor T cells highly express Slamf6 (Ly108) and are absent of CD39, a marker of terminal exhaustion of TIM-3$^+$ T cells. Over the course of PD1 therapy, exhausted T cells switch to a low expression of Slamf6 and high CD39 beyond 7 days[47]. We aimed to test mPET imaging with the radiolabelled antibodies [^{89}Zr]Zr-DFO-CD39 and [^{124}I]I-Ly108 in a HKP1 immunocompetent lung-cancer model to classify the state of T-cell exhaustion, which may potentially make for a PET diagnostic for checkpoint-blockade immunotherapy[46]. BLI imaging was done on day 3 to bracket mice into low, medium and high lung-tumour burden by s-rank for day 7 and day 14 post HKP1 implantation and mPET imaging. Day 7 imaging by mPET (48 h after immunoPET administration) identified two different antibody distributions, with higher uptake of [^{89}Zr]Zr-DFO-CD39 in the liver and spleen, alongside expected dehalogenation of [^{124}I]I-Ly108, with free iodine in the unblocked thyroid (Extended Data Fig. 4a). Little to no differentiation in PET uptake was seen in the lungs between CD39 and Ly108 or by disease burden initially. However, by day 14 (Extended Data Fig. 4b), increased [^{89}Zr]Zr-DFO-CD39 uptake was seen in the lungs. [^{124}I]I-Ly108 uptake was also increased on day 14 compared with day 7 in the liver and the spleen and in the abdominal cavity. Within the day 14 imaged mice, [^{124}I]I-Ly108 uptake in general decreased in the thoracic cavity with increasing tumour burden by BLI. Although individual tumour nodules could not be readily identified with these radiotracers owing to the inherent lower resolution of the PET system, lung tumour nodules could only be resolved by CT starting on day 14. Further studies are needed to refine CD39 and Ly108 with other immunoPET pairs to improve immune-checkpoint diagnostics. Yet mPET provided dual immunoPET radiotracer imaging in vivo showing degrees of T-cell infiltration and exhaustion with lung-cancer burden. The refinement of immunoPET alongside new labelling methods for isotope pairs may lead to improvements in mPET for the stratification of responders and non-responders undergoing chemotherapy or immunotherapy.

Outlook

Multiplexed PET is a generalized reconstruction method to separate two PET isotopes within a single PET acquisition solely on the basis of the type of gamma emission. mPET provides additional temporal information via the addition of a second tracer, and the method would greatly improve visualization when used with synchronized molecular imaging agents. By differentiating the additional isotope with the prompt gamma emission, mPET imaging can leverage many isotopes previously seen as problematic owing to their additional gamma emissions. In this study we have shown that both preclinical and clinical PET/CT systems can be easily adapted to perform mPET experiments while maintaining the quantitative power of PET. This is done without requiring any energy windowing to identify either isotope (as done with SPECT). We have used this method to address drug-loading and binary-distribution questions in addition to showing dual immune-marker quantitation. The mPET reconstruction method may allow researchers and clinicians to increase the density of information extracted from a single-PET imaging study. With increasing energy discrimination, mPET could lead to several-colour PET imaging, which would provide images with even richer information depth than the current single-colour state of PET imaging.

Methods

mPET imaging

Preclinical PET imaging was conducted on a Siemens Inveon PET/CT with a target acquisition count of greater than 60 million events per radiotracer per mouse, using an in-house-constructed four-position mouse hotel. Acquisition times were adjusted between 20 and 30 min depending on the activity injected (typically 4.6–5.2 MBq per mouse total at the time of imaging). The Inveon PET/CT scanner consists of a 20 × 20 array of lutetium oxyorthosilicate (LSO) crystals with a spatial resolution of 1.4 mm. The maximum energy window was typically set to 700 keV to maximize the detection of high-energy prompt γ-rays for ^{124}I and match the initial uniformity phantoms. The Inveon energy range can be expanded up to 814 keV to capture the largest number of events including the highest prompt gamma coincidence fraction[48] but would also include more random scatter events. Clinical PET imaging was performed with the generosity of the Cornell Citigroup Biomedical Imaging Center and their Siemens Biograph mCT. Uniformity and phantoms were acquired for 2,400 s under 64 bit mode. mCT acquisition produced the following: double prompt = 282.7 million counts, double randoms = 29.3 million counts, triple prompts = 10.39 million counts and triple randoms = 4.55 million counts. Attenuation was estimated from the co-registered CT image, scatter and spurious background with the fast Monte Carlo GPU code (MCGPU)-PET which can be found online at Github https://github.com/DIDSR/MCGPU-PET. List-mode data were processed producing doubles and triples datasets (Supplementary Fig. 11). Double coincidences were reconstructed using the standard MLEM algorithm (Supplementary Fig. 1b), while the triples used a modified version of MLEM (Supplementary Fig. 1c) available at https://github.com/jlherraiz/GFIRST. The separated images were obtained with an iterative algorithm based on the calibrated sensitivity of detecting double and triple coincidences for each radionuclide (Supplementary Fig. 1d), resulting in the final separated double (Supplementary Fig. 1e) and triple images (Supplementary Fig. 1f). A schema of the mPET separation process can be found in Fig. 2.

Reconstruction quantitation

Quantitative PET[28] imaging applied corrections in attenuation, scatter, random and spurious background from each isotope. Corrections are applied first to the sinogram of triple coincidences with an identical correction then applied to the doubles sinogram. Attenuation correction is obtained via the co-registered CT image, scatter and spurious background are obtained with the fast Monte Carlo method MCGPU-PET, and random triples are obtained directly from the delayed coincidences provided by the scanner as non-prompt-gamma coincidences are treated as random. With the energy resolution and energy window used, the contribution of triples caused by inter-detector scatter[24] was low, and scatter effects from contiguous detectors were not considered in the simulation. Typically, only a low percentage of the coincidences are triples, but these are of significantly higher abundance than random triples in the scanners tested. To mitigate the possible noise from a low triple-coincidence rate, a bilateral guided filter was also applied during the triples reconstruction. Finally, separated images of each isotope can be recovered considering the differences in sensitivity of triples versus doubles in each image voxel as estimated before in MCGPU-PET.

Computation time

List-mode data processing takes about 5 min for a 2 Gb file in 1 CPU. Next, the generated double and triple sinograms are reconstructed using an adapted version of an image reconstruction code written in C++/CUDA called GPU-FIRST. Sixty iterations are used with no subsets, requiring 5 min per sinogram (that is, 10 min in total for double and triple sinograms). In this implementation, an initial reconstruction with only attenuation and randoms correction (that is, without scatter and background correction) is applied, and then the simulator MCGPU-PET is used for the estimation of scatter and background. Therefore, the total reconstruction time is about 30 min per acquisition. Reconstruction time may be reduced by using subsets, estimating the scatter and background in the middle of the reconstruction (as it is commonly done in clinical scanners), instead of performing two reconstructions and performing the list-mode data processing with multiple CPUs.

Uniformity calibration and mouse phantom

A 1 l cylinder was used for uniformity measurement containing 5.2 MBq (140 µCi) of one of the following isotopes: ^{68}Ga, ^{18}F, ^{89}Zr, ^{86}Y, ^{76}Br and ^{124}I. Uniformity phantoms were measured for a minimum of 2 h. The mouse phantom was 3D printed by the Memorial Sloan Kettering Cancer Center department of Medical Physics containing an empty body cavity in addition to four external 1 ml tumour cavities. About 9.25 MBq (250 µCi) ^{89}Zr was inserted into the main body cavity, while mixtures of ^{89}Zr and either ^{76}Br, ^{86}Y or ^{124}I were added at the following amounts: 0 MBq and 2.22 MBq, 0.74 MBq and 1.42 MBq, 1.42 MBq and 0.74 MBq, and 2.22 MBq and 0 MBq. For the ^{124}I or ^{86}Y and ^{89}Zr combinations, the mPET energy range was increased from 350–650 keV to 350–700 keV and the phantom imaged for 30 min.

Small-molecule mPET and animal handling

[^{18}F]FDG was provided as need by the Radiochemistry and Molecular Imaging Probes Core and delivered at a concentration >1 mCi ml^{-1}. Synthesis of [^{124}I]I-trametinib was prepared as described previously[35]. Briefly, [^{124}I]I-trametinib was prepared from ~200 µg boronoato-trametinib precursor with 800 µg copper (II) chloride, between 37 MBq and 444 MBq (1–12 mCi) of ^{124}I, 1 mg of 1,10-phenanthroline in 4:1 methanol:water and heated for 30 min at 80 °C. The reaction mixture was purified by HPLC (Supplementary Fig. 12a) on an Atlantis T3 4.6 × 150 mm C18 analytical column over a 45 min 5–95% acetonitrile:water gradient with 0.01% trifluoroacetic acid. Synthesis and separation yielded a specific activity >100 MBq µmol^{-1} and HPLC fraction buffer exchanged via sep-pack light C18 cartridge for elution in pure ethanol for subsequent dilution for injection in saline. c57bl/6j mice bearing melanomas on their right flank were administered ~14.8 MBq (400 µCi) [^{124}I]I-trametinib intravenously and imaged at 24 h and 48 h later with the additional administration of ~7.4 MBq (200 µCi) [^{18}F]FDG respectively 1 h before imaging. c57bl/6j mice bearing B16F10 tumours (NCI-DTP catalogue number B16F10, RRID:CVCL_0159) were separated into therapy groups given via intraperitoneal injection of saline, trametinib 0.6 mg kg^{-1}, vemurafenib 1.2 mg kg^{-1} and trametinib 0.6 mg kg^{-1} with vemurafenib 1.2 mg kg^{-1} once daily for 3 days before radiotracer administration. Mice were made to fast 10 h before [^{18}F]FDG administration, with n = 4 mice per group. The energy window used was 350–700 keV, and the mice were imaged for 30 min. The experimental procedures were approved by the Institutional Animal Care and Use Committee of Memorial Sloan Kettering Cancer Center under protocol 08-07-014, and all animals were housed and cared for by Veterinary Services with attention to animal care and research ethics. NOD SCID gamma male mice and c57bl/6j female mice were obtained from Jackson Laboratories, while athymic nude female mice (outbred) were obtained from Charles River Laboratories.

[^{124}I]I-trametinib and [^{89}Zr]Zr-ferumoxytol

Iodinated trametinib as described previously[35] was made from a bora-pinacol trametinib precursor via copper-mediated insertion of ^{124}I. [^{89}Zr]Zr-ferumoxytol was produced via an adapted heat-induced radiolabelling method[40] where neutralized ^{89}Zr from oxalate is mixed with purified ferumoxytol (600 µg per mouse, 20 µl stock) from AMAG Pharmaceuticals, in 10 mM MES pH 8 buffer at 95 °C for 2 h. Subsequent purification and EDTA stripping removed unbound ^{89}Zr, and purity was determined by instant thin-layer chromatography (ITLC) to be >94% (Supplementary Fig. 12c). Radiotracers were injected in saline at an activity concentration of ~14.8 MBq (200 µCi) [^{124}I]I-trametinib and ~9.3 MBq (250 µCi) ^{89}Zr labelled onto 900 µg ferumoxytol. Loading

of [^{124}I]I-trametinib onto [^{89}Zr]Zr-ferumoxytol was achieved through the solvent diffusion method where [^{124}I]I-trametinib in DMSO is added dropwise into an aqueous solution of [^{89}Zr]Zr-ferumoxytol under rapid vortexing. Loading study variations to improve retention included heating, co-loading with cold trametinib in DMSO, or coating with bovine serum albumin on Amicon filters prior to loaded nanoparticle diafiltration. A c57bl/6j mouse bearing a B16F10 tumour on the right dorsal foot pad (NCI-DTP catalogue number B16F10, RRID:CVCL_0159) was then given a single injection of the loaded radiotracer as detailed above. PET acquisition for mPET was acquired using a 350–700 keV energy range for 30 min. The experimental procedures were approved by the Institutional Animal Care and Use Committee of Memorial Sloan Kettering Cancer Center under protocol 08-07-014, and all animals were housed and cared for by Veterinary Services with attention to animal care and research ethics.

T-cell exhaustion via mPET

Antibodies against murine CD39, clone Duha59 and slamf6 (Ly108), clone 330-AJ were obtained from Biolegend. CD39 antibody was conjugated with p-SCN-deferoxamine at pH 8.5–8.9 from Macrocyclics and subsequently purified via PD-10 column in Chelex grade PBS and concentrated for injection with an Amicon Ultra-0.5 30 kDa concentrator. Conjugated antibodies were subsequently radiolabelled with ^{89}Zr after neutralization in 1 M HEPES and heated for 1 h at 37 °C and characterized by ITLC in an EDTA mobile phase. Labelled antibodies were found to have a radiochemical purity exceeding 99% (Supplementary Fig. 12e) with a specific activity of >19 MBq per 100 µg. Iodination of slamf6 with ^{124}I was achieved via the IODOGEN method. Radiolabelling after PD-10 purification yielded an ITLC purity >95% (Supplementary Fig. 12f) with a specific activity >19 MBq per 100 µg. Mice were administered 1.5×10^5 HKP1 cells[49] intravenously for lung seeding and BLI tumour measurement on day 3 before S-rank sorting into groups for mPET imaging on days 7 and 14. mPET images were acquired at 24 h and 48 h post injection of 100 µg [^{89}Zr]Zr-DFO-CD39 and [^{124}I]I-Ly108. The mPET energy range was acquired at 350–700 keV, and mice were imaged for 30 min. The experimental procedures were approved by the Institutional Animal Care and Use Committee of Memorial Sloan Kettering Cancer Center under protocol 08-07-014, and all animals were housed and cared for by Veterinary Services with attention to animal care and research ethics.

CAR T-cell tracking of PSMA-positive tumours

NOD SCID gamma immunocompromised mice were subcutaneously implanted on the top shoulder flank with PSMA-positive (left) and PSMA-null (right) PC3 human prostate cancer cells. CAR T-cells and PSMA-positive and PSMA-negative cancer cells were previously engineered with three independent bioluminescence reporters, namely, membrane anchored *Cypridina* (maCluc), click beetle green and *Renilla* luciferases, respectively, thereby enabling the long-term in vivo BLI of all three populations within the same animal[9]. Characterization of CAR T-cells can be seen in Extended Data Fig. 2, with flow cytometry gating strategy in Supplementary Fig. 13. At 25 days post implantation, 1×10^6 hNIS.P28z.exCLuc CAR T were administered intravenously. In vivo tumour BLI was performed on days −4 and 18, whereas CAR T BLI was performed 1 day and 18 days post CAR-T injection and allowed a reliable assessment of CAR T targeting and homing at the tumour. At 8 days post CAR T administration, 10.4 MBq (280 µCi) ^{124}I (MSKCC radiochemistry and molecular imaging probes core or 3D imaging) was administered 2 h before mPET imaging, while 13.7 MBq [^{68}Ga]Ga-PSMA-11 was administered in addition 1 h before mPET imaging. [^{68}Ga]Ga-PSMA-11 was produced using gallium-68 from an Eckert and Ziegler manual generator and radiolabelled with PSMA-11 as described previously[50]. The mPET energy range was acquired at 350–700 keV with the mice imaged for 30 min. Ex vivo labelling of CAR T-cells was performed on the basis of previous ex vivo labelling methods for γδT and other immune cells[51,52] using a [^{89}Zr]Zr-Oxine labelling strategy of live cells. Briefly, ^{89}Zr was neutralized with sodium carbonate and diluted with water for addition of 10 mg ml^{-1} 8-hydroxyquinoline in chloroform as vortexed at maximum speed for 5 min. The solution was expanded with 450 µl of new chloroform and vortexed for an additional 10 min. The chloroform layer was extracted and dried under nitrogen at 60 °C before reconstitution into 20 µl DMSO. ITLC with ethyl acetate shows [^{89}Zr]Zr-Oxine product traveling with the mobile phase and a purity >97% (Supplementary Fig. 12d). NOD SCID gamma immunocompromised mice were implanted on the top shoulder flank with PSMA-positive (left) and PSMA-null (right) PC3 prostate cancer cells. At 4 weeks post implantation, [^{89}Zr]Zr-Oxine labelled CAR T-cells (709 model, 0.74 MBq (20 µCi) per 1×10^7 cells) were administered intravenously and imaged after 24 h. Yttrium-86 (MD Anderson Cyclotron) was neutralized in 150 mM ammonium acetate buffer pH 5 before addition of DOTA-PSMA precursor and subsequent heating at 90 °C for 30 min. ^{86}Y-DOTA-PSMA was purified by HPLC (Supplementary Fig. 12b) using an Atlantis C18 analytical column over a 5–95% acetonitrile:water gradient with 0.1% trifluoroacetic acid. HPLC fraction was buffer exchanged on an Oasis HLB cartridge before elution with ethanol, drying with argon and re-suspending in PBS. ^{86}Y-DOTA-PSMA 2.4 MBq (65 µCi) per 4 µg was administered 2 h before the 24 h CAR-T imaging timepoint via retro-orbital injection. mPET imaging was conducted in a single 20 min PET/CT scan using the modified energy window of 350–814 keV. Unique biological materials are available from the authors upon reasonable request.

Reporting summary

Further information on research design is available in the Nature Portfolio Reporting Summary linked to this article.

Data availability

The main data supporting the results in this study are available within the paper and its Supplementary Information. Source Data and sinograms for the phantoms in Fig. 3 are available at https://doi.org/10.5281/zenodo.8034519 while figures are available from figshare with the identifier https://doi.org/10.6084/m9.figshare.21816069.

Code availability

The mPET code consists of several modules, requiring access to additional code considered proprietary to the PET-scanner manufacturers (although for PET/CT systems such as the Siemens Inveon, it can be made available in a compiled version). In addition, the software requires hands-on training for implementation, which can be made available on reasonable request. The Monte Carlo code, MCGPU-PET, can be accessed via Github at https://github.com/DIDSR/MCGPU-PET, whereas code for reconstructing doubles and triples can also be accessed via https://github.com/jlherraiz/GFIRST. Isotope separation is determined from phantom studies performed on each scanner and isotope pair used.

References

1. DeBerardinis, R. J. & Chandel, N. S. We need to talk about the Warburg effect. *Nat. Metab.* **2**, 127–129 (2020).
2. Black, N. F., McJames, S. & Kadrmas, D. J. Rapid multi-tracer PET tumor imaging with F-FDG and secondary shorter-lived tracers. *IEEE Trans. Nucl. Sci.* **56**, 2750–2758 (2009).
3. Marti-Climent, J. M. et al. Effective dose estimation for oncological and neurological PET/CT procedures. *EJNMMI Res.* **7**, 37 (2017).
4. Farber, D. L. Tissues, not blood, are where immune cells function. *Nature* **593**, 506–509 (2021).
5. Heinzmann, K., Carter, L. M., Lewis, J. S. & Aboagye, E. O. Multiplexed imaging for diagnosis and therapy. *Nat. Biomed. Eng.* **1**, 697–713 (2017).
6. Andreou, C., Weissleder, R. & Kircher, M. F. Multiplexed imaging in oncology. *Nat. Biomed. Eng.* **6**, 527–540 (2022).
7. Zanzonico, P. Principles of nuclear medicine imaging: planar, SPECT, PET, multi-modality, and autoradiography systems. *Radiat. Res.* **177**, 349–364 (2012).

8. Ko, J. et al. Spatiotemporal multiplexed immunofluorescence imaging of living cells and tissues with bioorthogonal cycling of fluorescent probes. *Nat. Biotechnol.* **40**, 1654–1662 (2022).
9. Moroz, M. A. et al. Introducing a new reporter gene, membrane-anchored *Cypridina* luciferase, for multiplex bioluminescence imaging. *Mol. Ther. Oncolytics* **21**, 15–22 (2021).
10. Yagishita, A. et al. Simultaneous visualization of multiple radionuclides in vivo. *Nat. Biomed. Eng.* **6**, 640–647 (2022).
11. Yang, M. et al. Multiplexed PET probes for imaging breast cancer early response to VEGF121/rGel treatment. *Mol. Pharmaceutics* **8**, 621–628 (2011).
12. Bell, C. et al. Dual acquisition of18F-FMISO and18F-FDOPA. *Phys. Med. Biol.* **59**, 3925–3949 (2014).
13. Andreyev, A. & Celler, A. Dual-isotope PET using positron-gamma emitters. *Phys. Med. Biol.* **56**, 4539–4556 (2011).
14. Herraiz, J. L. et al. GPU-based fast iterative reconstruction of fully 3-D PET sinograms. *IEEE Trans. Nucl. Sci.* **58**, 2257–2263 (2011).
15. Carter, L. M. et al. The impact of positron range on PET resolution, evaluated with phantoms and PHITS Monte Carlo simulations for conventional and non-conventional radionuclides. *Mol. Imaging Biol.* https://doi.org/10.1007/s11307-019-01337-2 (2019).
16. Cal-González, J. et al. Positron range effects in high resolution 3D PET imaging. In *2009 IEEE Nuclear Science Symposium Conference Record (NSS/MIC)*, 2788-2791 https://doi.org/10.1109/NSSMIC.2009.5401950 (2009).
17. Lubberink, M. & Herzog, H. Quantitative imaging of ^{124}I and ^{86}Y with PET. *Eur. J. Nucl. Med. Mol. Imaging* **38**, S10–S18 (2011).
18. Kull, T., Ruckgaber, J., Weller, R., Reske, S. & Glatting, G. Quantitative imaging of yttrium-86 PET with the ECAT EXACT HR$^+$ in 2D mode. *Cancer Biother. Radiopharm.* **19**, 482–490 (2004).
19. Lubberink, M., Schneider, H., Bergström, M. & Lundqvist, H. Quantitative imaging and correction for cascade gamma radiation of ^{76}Br with 2D and 3D PET. *Phys. Med. Biol.* **47**, 3519–3534 (2002).
20. Beattie, B. J., Finn, R. D., Rowland, D. J. & Pentlow, K. S. Quantitative imaging of bromine-76 and yttrium-86 with PET: a method for the removal of spurious activity introduced by cascade gamma rays. *Med. Phys.* **30**, 2410–2423 (2003).
21. Watson, C. C., Newport, D. & Casey, M. E. In *Three-Dimensional Image Reconstruction in Radiology and Nuclear Medicine* (eds Grangeat, P. & Amans, J.-L.) 255–268 (Springer, 1996).
22. Sanaat, A. et al. Deep learning-assisted ultra-fast/low-dose whole-body PET/CT imaging. *Eur. J. Nucl. Med. Mol. Imaging* **48**, 2405–2415 (2021).
23. Jung, K. O. et al. Whole-body tracking of single cells via positron emission tomography. *Nat. Biomed. Eng.* **4**, 835–844 (2020).
24. Cal-Gonzalez, J. et al. Simulation of triple coincidences in PET. *Phys. Med. Biol.* **60**, 117–136 (2015).
25. Lage, E. et al. Recovery and normalization of triple coincidences in PET. *Med. Phys.* **42**, 1398–1410 (2015).
26. Surti, S., Scheuermann, R. & Karp, J. S. Correction technique for cascade gammas in I-124 imaging on a fully-3D, time-of-flight PET scanner. *IEEE Trans. Nucl. Sci.* **56**, 653–660 (2009).
27. Preylowski, V. et al. Is the image quality of I-124-PET impaired by an automatic correction of prompt gammas? *PLoS ONE* **8**, e71729 (2013).
28. Surti, S. & Scheuermann, J. In *Physics of PET and SPECT Imaging* Ch. Data corrections and quantitative PET, 24 (CRC, 2017).
29. Ilisie, V. et al. High resolution and sensitivity gamma camera with active septa. A first Monte Carlo study. *Sci. Rep.* **9**, 18431 (2019).
30. Andreyev, A., Sitek, A. & Celler, A. EM reconstruction of dual isotope PET using staggered injections and prompt gamma positron emitters. *Med. Phys.* **41**, 022501 (2014).
31. Fukuchi, T. et al. Image reconstruction method for dual-isotope positron emission tomography. *J. Instrum.* **16**, P01035–P01035 (2021).
32. Beekman, F. J., Kamphuis, C., Koustoulidou, S., Ramakers, R. M. & Goorden, M. C. Positron range-free and multi-isotope tomography of positron emitters. *Phys. Med. Biol.* **66**, 065011 (2021).
33. Kaittanis, C. et al. Environment-responsive nanophores for therapy and treatment monitoring via molecular MRI quenching. *Nat. Commun.* **5**, 3384 (2014).
34. Volpe, A. et al. Spatiotemporal PET imaging reveals differences in CAR-T tumor retention in triple-negative breast cancer models. *Mol. Ther.* **28**, 2271–2285 (2020).
35. Pratt, E. C. et al. Synthesis of novel PET tracer 124I-trametinib for MAPK/ERK kinase distribution and resistance monitoring. *J. Nucl. Med.* https://doi.org/10.2967/jnumed.120.241901 (2020).
36. Parmenter, T. J. et al. Response of BRAF-mutant melanoma to BRAF inhibition is mediated by a network of transcriptional regulators of glycolysis. *Cancer Discov.* **4**, 423–433 (2014).
37. Hrkach, J. & Langer, R. From micro to nano: evolution and impact of drug delivery in treating disease. *Drug Deliv. Transl. Res.* **10**, 567–570 (2020).
38. Thorek, D. L. et al. Non-invasive mapping of deep-tissue lymph nodes in live animals using a multimodal PET/MRI nanoparticle. *Nat. Commun.* **5**, 3097 (2014).
39. Yuan, H. et al. Heat-induced radiolabeling and fluorescence labeling of Feraheme nanoparticles for PET/SPECT imaging and flow cytometry. *Nat. Protoc.* **13**, 392–412 (2018).
40. Boros, E., Bowen, A. M., Josephson, L., Vasdev, N. & Holland, J. P. Chelate-free metal ion binding and heat-induced radiolabeling of iron oxide nanoparticles. *Chem. Sci.* **6**, 225–236 (2015).
41. *MEKINIST (Trametinib) (Package Insert)*. (GlaxoSmithKline, 2019).
42. Sarrett, S. M. et al. Inverse electron demand Diels–Alder click chemistry for pretargeted PET imaging and radioimmunotherapy. *Nat. Protoc.* **16**, 3348–3381 (2021).
43. Zeglis, B. M. et al. Modular strategy for the construction of radiometalated antibodies for positron emission tomography based on inverse electron demand Diels–Alder click chemistry. *Bioconjug. Chem.* **22**, 2048–2059 (2011).
44. Tavare, R. et al. Engineered antibody fragments for immuno-PET imaging of endogenous CD8+ T cells in vivo. *Proc. Natl Acad. Sci. USA* **111**, 1108–1113 (2014).
45. Tavare, R. et al. An effective immuno-PET imaging method to monitor CD8-dependent responses to immunotherapy. *Cancer Res.* **76**, 73–82 (2016).
46. Miller, B. C. et al. Subsets of exhausted CD8(+) T cells differentially mediate tumor control and respond to checkpoint blockade. *Nat. Immunol.* **20**, 326–336 (2019).
47. Kallies, A., Zehn, D. & Utzschneider, D. T. Precursor exhausted T cells: key to successful immunotherapy? *Nat. Rev. Immunol.* **20**, 128–136 (2020).
48. Yu, A. R., Kim, H.-J., Lim, S. M. & Kim, J. S. Comparison of imaging characteristics of ^{124}I PET for determination of optimal energy window on the Siemens Inveon PET. *BioMed. Res. Int.* **2016**, 3067123 (2016).
49. Choi, H. et al. Transcriptome analysis of individual stromal cell populations identifies stroma–tumor crosstalk in mouse lung cancer model. *Cell Rep.* **10**, 1187–1201 (2015).
50. Ebenhan, T. et al. Development of a single vial kit solution for radiolabeling of ^{68}Ga-DKFZ-PSMA-11 and its performance in prostate cancer patients. *Molecules* **20**, 14860–14878 (2015).
51. Man, F. et al. In vivo PET tracking of ^{89}Zr-labeled Vγ9Vδ2 T cells to mouse xenograft breast tumors activated with liposomal alendronate. *Mol. Ther.* **27**, 219–229 (2019).
52. Man, F., Khan, A. A., Carrascal-Minino, A., Blower, P. J. & de Rosales, R. T. M. A kit formulation for the preparation of [^{89}Zr]Zr(oxinate)$_4$ for PET cell tracking: white blood cell labelling and comparison with [^{111}In]In(oxinate)$_3$. *Nucl. Med. Biol.* **90-91**, 31–40 (2020).

Acknowledgements

We thank D. Bauer of the Lewis Lab for their timely production of [^{68}Ga]Ga-PSMA-11, and V. Longo and P. Zanzonico of the Small Animal Imaging Core (MSKCC) for their support maintaining the Inveon PET/CT. We also thank E. Fung and M. Du of the Citigroup Biomedical Imaging Center (Weill Cornell) for their availability and operation of the Biograph mCT clinical PET/CT and M. Conti from Siemens for their direction on how to acquire 64-bit data with the mCT. In addition, we thank E. Lage, V. Parot, S. R. Dave, S. C. Moore and the Madrid-MIT m+Vision Consortium for their help with the initial steps in the development of the mPET method. This work was supported in parts by the following grants: National Institutes of Health R01 CA215700 and R01 EB033000 (to J.G.), R01 CA220524-01A1 (to V.P.), R01 CA204924 (to V.P.), R21 CA250478 (to V.P.), S10 OD016207-01 (to P. Zanzonico, MSKCC), and P30 CA08748 (to S. M. Vickers MSKCC). A.V. is supported by The Center for Experimental Immuno-Oncology Fellowship Award (FP00001443, Memorial Sloan Kettering Cancer Center). E.C.P. is currently supported by the National Institutes of Health F32 CA268912-01. J.L.H. is currently supported by the Spanish Ministry of Science and Innovation (MCIN) (PID2021-126998OB-I00, PDC2022-133057-I00/AEI/10.13039/501100011033/ Unión Europea Next GenerationEU/PRTR). J.M.U. is currently supported by the Spanish Ministry of Science and Innovation (MCIN) (PID2021-126998OB-I00).

Author contributions

E.C.P., A.L.M., A.V., M.J.C. and L.M.C. conducted and planned experiments, analysed data and wrote the manuscript. V.M., N.P., V.P, J.M.U., J.G. and J.L.H. designed experiments, analysed data and wrote the manuscript.

Competing interests

The authors declare no competing interests.

Additional information

Extended data is available for this paper at https://doi.org/10.1038/s41551-023-01060-y.

Supplementary information The online version contains supplementary material available at https://doi.org/10.1038/s41551-023-01060-y.

Correspondence and requests for materials should be addressed to Jan Grimm or Joaquin L. Herraiz.

Peer review information *Nature Biomedical Engineering* thanks Huafeng Liu, Bertrand Tavitian and the other, anonymous, reviewer(s) for their contribution to the peer review of this work. Peer reviewer reports are available.

https://doi.org/10.1038/s41551-023-01060-y

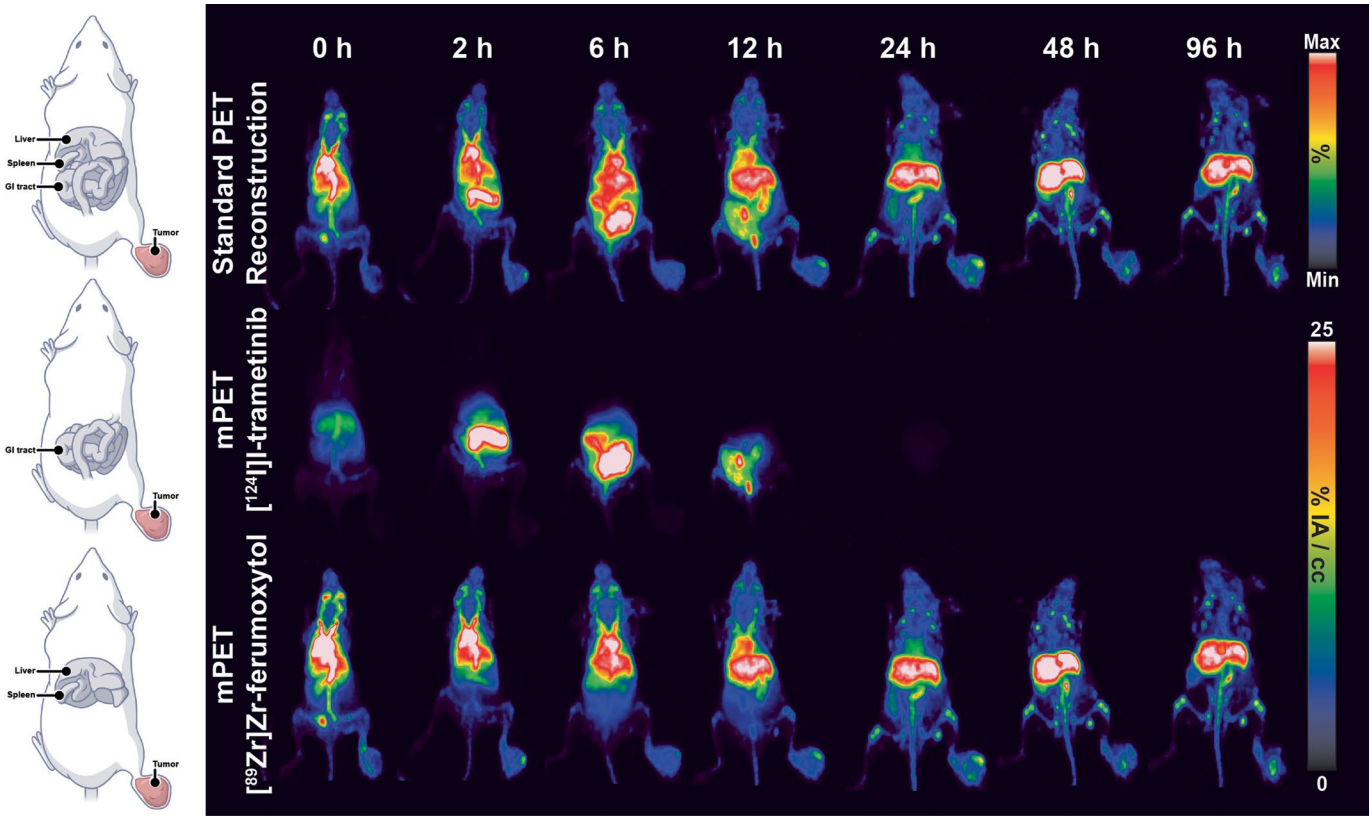

Extended Data Fig. 1 | Extended mPET imaging of nanoparticle biodistribution through 96 hours. Including data from Fig. 5 and extending through 96 hours. No change in biodistribution seen by standard reconstruction or mPET between 24 and 96 hours. %IA/CC represents percent injected activity per cubic centimetre.

https://doi.org/10.1038/s41551-023-01060-y

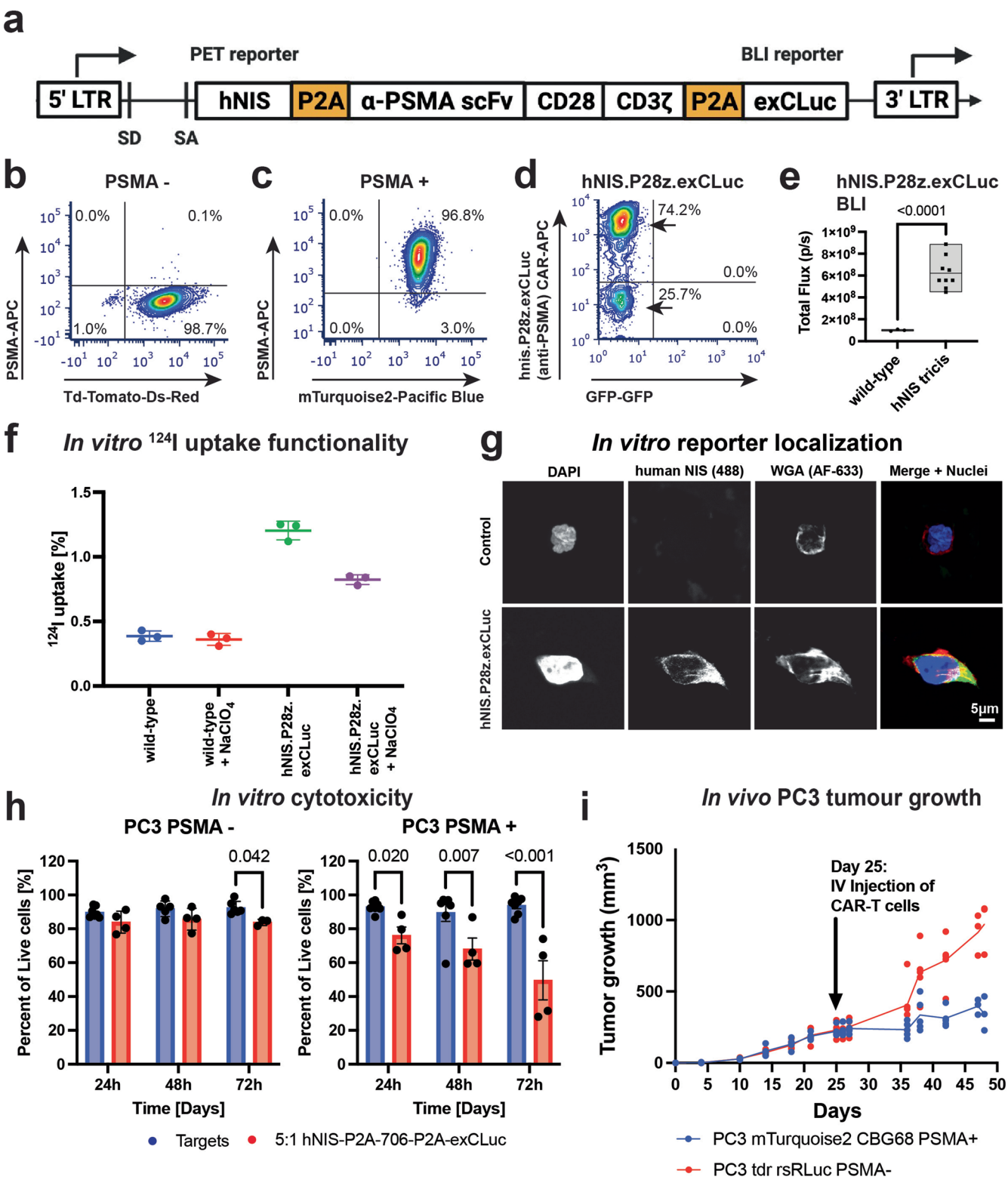

Extended Data Fig. 2 | See next page for caption.

https://doi.org/10.1038/s41551-023-01060-y

Extended Data Fig. 2 | Characterization of the tricistronic CAR T-cell PET-reporter system. Gene map of PET and reporter genes for CAR T cells containing the sodium Iodide symporter (hNIS), PSMA targeting scFv (P28z), and a BLI reporter system (exCLuc) to produce the CAR-T-cell hNIS.P28z.exCLuc. **b**, Flow plot of PC3 cells engineered lacking PSMA. **c**, PSMA-positive engineered cells. **d**, Flow plot of CAR T cells expressing the anti-PSMA-scFv. **e**, *In vitro* activation of the BLI reporter in tricistronic CAR T cells shows functional incorporation of the genes. **f**, Addition of ^{124}I to wild-type or tricistronic CAR T cells shows an increase with only tricistronic CAR T cells, with mild blocking with sodium perchlorate, confirming the specific uptake of ^{124}I through hNIS. **g**, Confocal imaging of wild-type and hNIS tricistronic CAR-T cells for nuclear staining, hNIS and WGA (wheat germ agglutinin). Scale bar, 5 µm. **h**, *In vitro* cytotoxicity of PSMA targeting CAR-T cells reduces cell population in PSMA-positive co-cultures, whereas PSMA-null cells were unaffected through 48 hours by the co culture with CAR-T cells. **I**, *In vivo* delivery of CAR T cells targeting PSMA-positive tumours led to reduced tumour growth in PSMA-positive tumours, whereas PSMA-negative tumours continued to grow. In **e**, **f**, **h**, **I**, the lines denote the mean with error bars representing the s.e.m. **b**-**d**, Representative flow-cytometry contour quadrant plot to show cell-intensity characteristics. The gating scheme can be found in Supplementary Fig. 11. **e**, Box plot representing min and max values, with the middle line as the mean. In **f**, **h**, n = 3 technical replicates per condition. In **i**, n = 5 mice per arm. In **e**,**h**, the *P* values are significant, using a multiple-comparison unpaired *t*-test and assuming the same s.d. in the population. %IA/CC represents percent injected activity per cubic centimetre.

https://doi.org/10.1038/s41551-023-01060-y

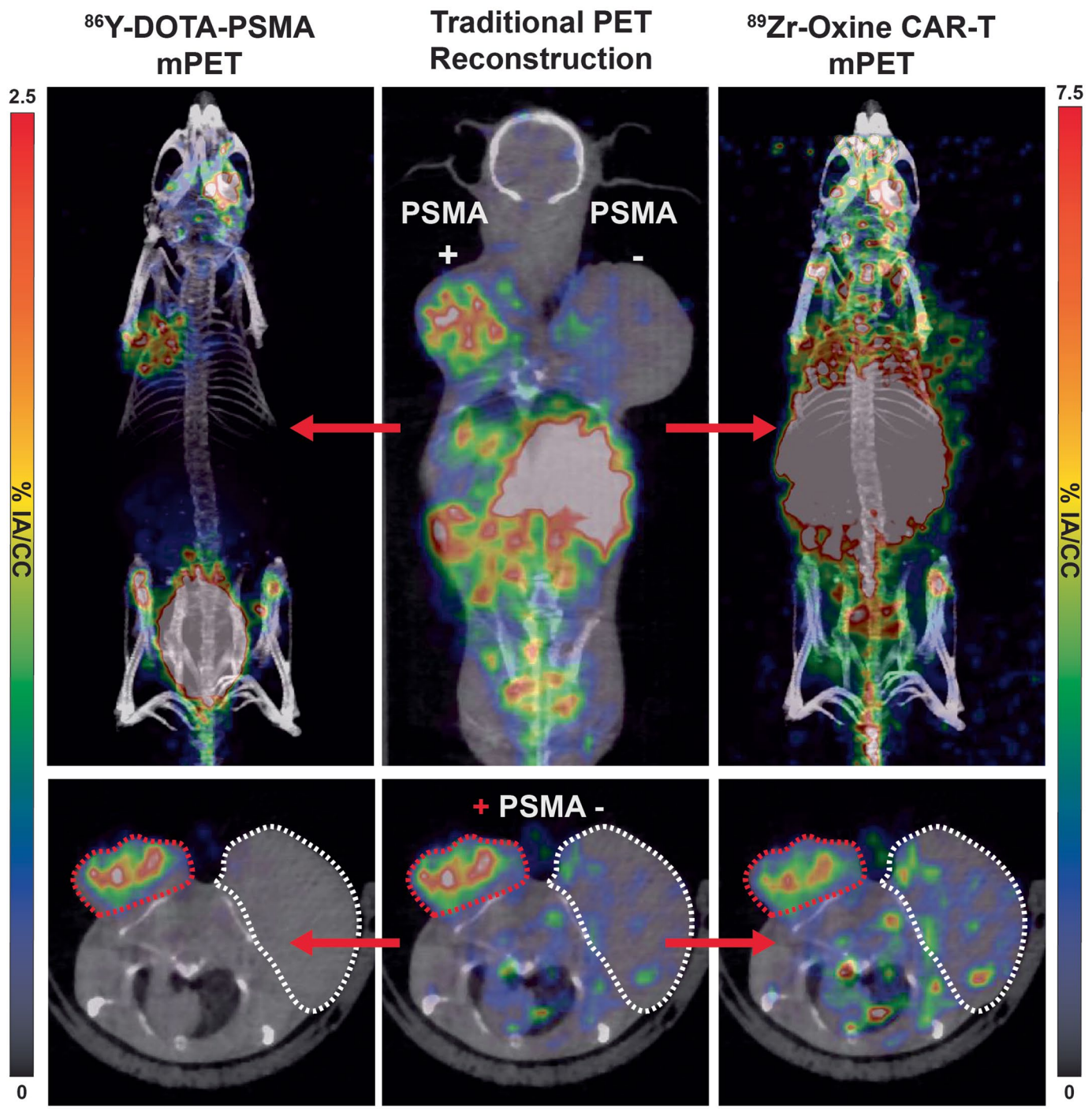

Extended Data Fig. 3 | Alternative ex vivo labelling of CAR T-cells with [^{89}Zr] Zr-Oxine and PSMA imaging with [^{86}Y]Y-DOTA-PSMA. [^{86}Y]Y-DOTA-PSMA / [^{89}Zr]Zr-oxine CAR T-cell mPET was found to have uptake of both PSMA-11 and CAR T -cell tracers in the PSMA-positive tumour (**left**), whereas minor to no activity was observed in both tracers for the PSMA-null tumour (**right**). Distribution of the [^{86}Y]Y-DOTA-PSMA tracer can be seen in the PSMA-positive tumour, in the ocular cavity where injected, and in the bladder during excretion. [^{89}Zr]Zr-oxine CAR T-cells were observed in the PSMA-positive tumour as well as in the liver and bone. Images were calibrated to a maximal 2.5 %IA/CC for [^{86}Y] Y-DOTA-PSMA and 7.5 %IA/CC for [^{89}Zr]Zr-oxine CAR T-cells. We used one mouse. %IA/CC represents percent injected activity per cubic centimetre.

https://doi.org/10.1038/s41551-023-01060-y

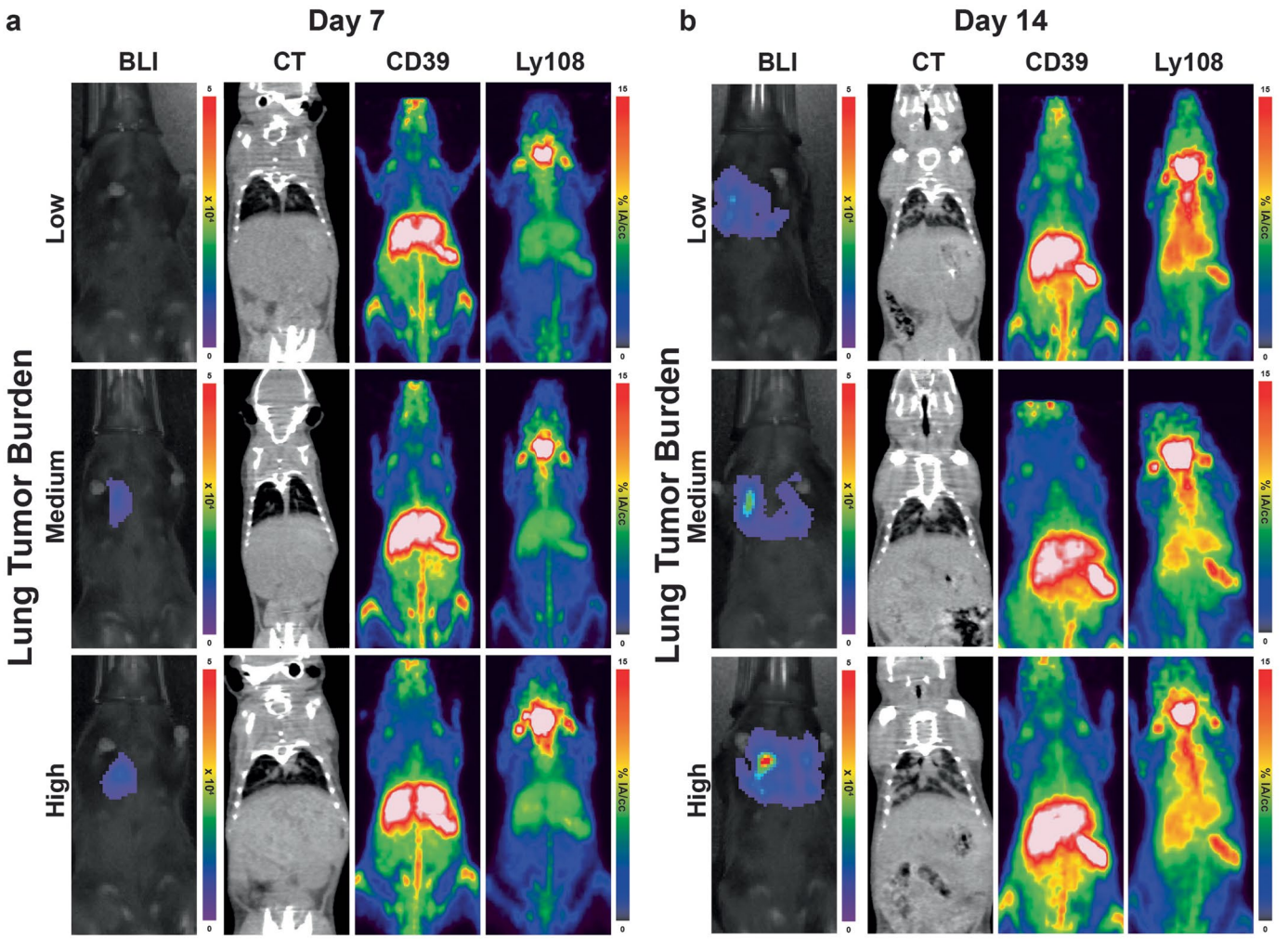

Extended Data Fig. 4 | mPET for developing immunoPET detection of T-cell exhaustion. Mice bearing HKP1 lung tumours were monitored for terminal and progenitor T-cell exhaustion using antibodies against CD39 or Ly108 during disease progression. BLI of lung tumour burden was measured prior to injection, with representative CT slice in thoracic cavity showing potential branch occlusions (bright spots off alveolar bifurcation). Ly108, a marker of effector T cells, decreased with disease burden whereas CD39, a marker of severely exhausted T cells, increased, according to flow-cytometry data. mPET imaging with [^{89}Zr]Zr-DFO-CD39 and [^{124}I]I-Ly108 at day 7 and day 14 with three levels of tumour burden. At day 7 no discernible difference between low, medium or high tumour burden in mice is seen with either [^{89}Zr]Zr-DFO-CD39 or [^{124}I]I-Ly108. By day 14, BLI shows an appreciable increase in tumour burden in all mice, with tumour occlusions seen on CT. By mPET there was a general increase in [^{89}Zr]Zr-DFO-CD39 and [^{124}I]I-Ly108 uptake in the lungs compared to the day-7 group. Less lung uptake was visible with [^{124}I]I-Ly108, with increasing tumour burden in the day-14 imaged mice. mPET again could separate two radiotracers *in vivo* and could be used with further radiotracer engineering to define T-cell exhaustion. N = 3 mice imaged per week (n = 6 total cohort), with each mouse receiving simultaneously [^{89}Zr]Zr-DFO-CD39 and [^{124}I]I-Ly108 by intravenous injection 48 hours prior to mPET. %IA/CC represents percent injected activity per cubic centimetre.

nature portfolio

Corresponding author(s): Jan Grimm and Joaquin Lopez Herraiz

Last updated by author(s): May 10, 2023

Reporting Summary

Nature Portfolio wishes to improve the reproducibility of the work that we publish. This form provides structure for consistency and transparency in reporting. For further information on Nature Portfolio policies, see our Editorial Policies and the Editorial Policy Checklist.

Statistics

For all statistical analyses, confirm that the following items are present in the figure legend, table legend, main text, or Methods section.

n/a	Confirmed
☐	☒ The exact sample size (*n*) for each experimental group/condition, given as a discrete number and unit of measurement
☐	☒ A statement on whether measurements were taken from distinct samples or whether the same sample was measured repeatedly
☐	☒ The statistical test(s) used AND whether they are one- or two-sided *Only common tests should be described solely by name; describe more complex techniques in the Methods section.*
☐	☒ A description of all covariates tested
☐	☒ A description of any assumptions or corrections, such as tests of normality and adjustment for multiple comparisons
☐	☒ A full description of the statistical parameters including central tendency (e.g. means) or other basic estimates (e.g. regression coefficient) AND variation (e.g. standard deviation) or associated estimates of uncertainty (e.g. confidence intervals)
☐	☒ For null hypothesis testing, the test statistic (e.g. *F*, *t*, *r*) with confidence intervals, effect sizes, degrees of freedom and *P* value noted *Give P values as exact values whenever suitable.*
☒	☐ For Bayesian analysis, information on the choice of priors and Markov chain Monte Carlo settings
☒	☐ For hierarchical and complex designs, identification of the appropriate level for tests and full reporting of outcomes
☒	☐ Estimates of effect sizes (e.g. Cohen's *d*, Pearson's *r*), indicating how they were calculated

Our web collection on statistics for biologists contains articles on many of the points above.

Software and code

Policy information about availability of computer code

Data collection	PET data were collected through the Inveon Acquisition Workstation, Version 2.2.2.1050. Siemens Biograph mCT data were acquired through the server command line in 64-bit mode. Bioluminescence images were acquired with a Perkin-Elmer IVIS Living Image V.4.3.1
Data analysis	PET listmode data processed using the custom mPET algorithm in conjunction with Monte Carlo, MCGPU-PET, can be accessed on Github at https://github.com/DIDSR/MCGPU-PET. Double-isotope and triple-isotope separation code can be accessed on Github at https://github.com/jlherraiz/GFIRST. Separated and calibrated PET images were viewed and exported in Inveon Research Workstation V4, Launcher 4.0.1.1. Data analysis was performed on Prism 9 for MacOS, V 9.4.0 (453).

For manuscripts utilizing custom algorithms or software that are central to the research but not yet described in published literature, software must be made available to editors and reviewers. We strongly encourage code deposition in a community repository (e.g. GitHub). See the Nature Portfolio guidelines for submitting code & software for further information.

Data

Policy information about availability of data

All manuscripts must include a data availability statement. This statement should provide the following information, where applicable:

- Accession codes, unique identifiers, or web links for publicly available datasets
- A description of any restrictions on data availability
- For clinical datasets or third party data, please ensure that the statement adheres to our policy

The main data supporting the results in this study are available within the paper and its Supplementary Information. All data generated in this study, including source data for the figures, are available from figshare with the identifier https://doi.org/10.6084/m9.figshare.21816069.

Human research participants

Policy information about studies involving human research participants and Sex and Gender in Research.

Reporting on sex and gender	The study did not involve human research participants.
Population characteristics	—
Recruitment	—
Ethics oversight	—

Note that full information on the approval of the study protocol must also be provided in the manuscript.

Field-specific reporting

Please select the one below that is the best fit for your research. If you are not sure, read the appropriate sections before making your selection.

☒ Life sciences ☐ Behavioural & social sciences ☐ Ecological, evolutionary & environmental sciences

For a reference copy of the document with all sections, see nature.com/documents/nr-reporting-summary-flat.pdf

Life sciences study design

All studies must disclose on these points even when the disclosure is negative.

Sample size	No sample-size calculated was performed. For in vivo imaging, a group size of n = 4 was used for Fig. 4, as up to 4 mice can be loaded into the PET scanner at one time. For Fig. 6, n = 5 mice were used for imaging, as the cage could house up to 5 mice. For Fig. 6, n = 4 mice were scanned for session one, and n = 1 for session two. Injections were staggered for mouse 5 to allow the same radiotracer distribution time at the start of imaging for each session. For Fig. 5, n = 1 one mouse was scanned, as the mouse holder had not been fabricated. For Supplementary Fig. 8, n = 1 mouse was scanned, as only one mouse was available, and availability of 86Y-DOTA-PSMA was limiting. For Supplementary Fig. 9, n = 3 mice were injected with a combined radiotracer-activity limit for the scanner (~1.2mCi). n = 3 mice were maintained for both weeks of imaging to ensure similar radiotracer-specific activity and total activity amount.
Data exclusions	No mice or phantoms were excluded from acquisition or from analysis.
Replication	Replication is shown in Supplementary Fig. 5e, with similar biodistributions of both isotopes one week after first radiotracer injection. All other experiments shown included a cohort of 4–5 mice (except for Fig. 5, where n = 1) per group to show inter-mouse variation in biodistribution. In general, replicates were not done by default, as imaging cohorts covered several time points and the experiments are expensive to repeat outright, given the cost of the radiotracer and of instrument reservation. However, as stated, multiple mice were used for each study group.
Randomization	Randomization was only performed for Extended Data Fig. 4, by S-rank by lung BLI intensity, so each weekly cohort had low, mid or high BLI. Mice in Fig. 4 were randomly sorted into one of four cages, after which the mice were put onto trametinib, vemurafenib, both or saline before imaging. Regardless, all mice received the same radiotracer combination. In all other studies, all mice were injected with identical amounts of the given radiotracer pair without any randomization.
Blinding	No blinding was done during any experiment, as the majority of radiotracers selected for this study have been tested in similar models and are known to target the epitope present in the tumour tissue. The dual CD39 Ly108 antibody imaging was performed on the basis of flow-cytometry data reported in another model. For mPET separation and analysis, the studies were partially blinded, whereby listmode PET data was sent for mPET separation alongside only the amount of each radiotracer injected per mouse for calibration.

Reporting for specific materials, systems and methods

We require information from authors about some types of materials, experimental systems and methods used in many studies. Here, indicate whether each material, system or method listed is relevant to your study. If you are not sure if a list item applies to your research, read the appropriate section before selecting a response.

Materials & experimental systems

n/a	Involved in the study
☐	☒ Antibodies
☐	☒ Eukaryotic cell lines
☒	☐ Palaeontology and archaeology
☐	☒ Animals and other organisms
☒	☐ Clinical data
☒	☐ Dual use research of concern

Methods

n/a	Involved in the study
☒	☐ ChIP-seq
☐	☒ Flow cytometry
☒	☐ MRI-based neuroimaging

Antibodies

Antibodies used	Details of the antibodies used for in vivo imaging are provided in Supplementary Table 2.
Validation	The antibodies CD39 and Ly108 were validated for use in flow cytometry by Biolegend, but subsequently lightly modified with the chelator DFO for 89Zr or directly iodinated with 124I, and used in vivo.

Eukaryotic cell lines

Policy information about cell lines and Sex and Gender in Research

Cell line source(s)	The cell lines used in this study, with source and gender, are described in Supplementary Table 3.
Authentication	The cell lines were authenticated by STR profiling, with the subsequent reporter-gene modification characterized and managed by each collaborator. CAR-T-cell characterization can be found in Extended Data Fig. 3.
Mycoplasma contamination	The cell lines were tested, and found to be free of mycoplasma contamination.
Commonly misidentified lines (See ICLAC register)	No commonly misidentified cells lines were used.

Animals and other research organisms

Policy information about studies involving animals; ARRIVE guidelines recommended for reporting animal research, and Sex and Gender in Research

Laboratory animals	6–8-week-old (for Extended Data Fig. 4) and 8–10-week-old C57/bl6J female mice (For Figs. 4 and 5), and 12–14-week-old male NOD-SCID Gamma mice (for Fig. 6 and Extended Data Fig. 3).
Wild animals	The study did not involve wild animals.
Reporting on sex	Sex was selected on the basis of the animal model used; male mice for prostate cancer, and female mice otherwise.
Field-collected samples	The study did not involve samples collected from the field.
Ethics oversight	The animal studies were approved by the MSKCC IACUC, under protocol 08-07-014.

Note that full information on the approval of the study protocol must also be provided in the manuscript.

Flow Cytometry

Plots

Confirm that:

☒ The axis labels state the marker and fluorochrome used (e.g. CD4-FITC).

☒ The axis scales are clearly visible. Include numbers along axes only for bottom left plot of group (a 'group' is an analysis of identical markers).

☒ All plots are contour plots with outliers or pseudocolor plots.

☒ A numerical value for number of cells or percentage (with statistics) is provided.

Methodology

Sample preparation	1x10^5 PC3 human prostatic adenocarcinoma cells previously engineered to express either PSMA+/mTurquoise2+/Click Beatle Green+ or PSMA-/Td-Tomato+/Renilla Luciferase+, as well as anti-PSMA (P28z) CAR-T cells expressing GFP fluorescent protein were washed twice with PBS and resuspended in FACS buffer (PBS pH 7.4 with 10% (v/v) FCS). Cancer cells were stained with a mouse anti-human PSMA monoclonal antibody (10 ug/mL; MBL #K0142-3, mouse IgG1 clone 107-1A4) and a polyclonal goat anti-mouse Ig secondary antibody conjugated to APC (2 ug/mL; BD Pharmigen, #550826). P28z CAR-T cells were stained using a goat anti-human IgG-biotinylated polyclonal antibody (0.5 ug/mL; SouthernBiotech, #2040-08) and APC Streptavidin secondary antibody (0.2 ug/mL; BD Pharmigen, #554067). All cells were stained for 1 hour at 4 °C in FACS buffer. Untransduced cell samples unstained, stained with primary and secondary antibodies and only with indicated secondary antibodies, were used as controls.
Instrument	LSRFortessa II (BD Bioscience, USA)
Software	The LSRFortessa II (BD Bioscience, USA) was equipped with a FACSDiva analysis software (BD Bioscience, version 8.0.1). Data analysis was performed using FCS Express (De Novo Software, version 7.14.0020).
Cell population abundance	Targeted cancer cells retrovirally engineered to express the desired transgenes were subjected to fluorescence-activated cell sorting (FACS) to select for positively transduced cells. Post-sort fraction of the relevant population within the sorting gate was >95%, as determined by flow cytometric analysis post-sort.
Gating strategy	Gating single steps for Supplementary Figure 13: 1) Forward (FSC) and side scatter (SSC) gating were used to identify the cell population of interest on the basis of size and granularity, respectively; 2) Side scatter width (SSC-W) versus side scatter height (SSC-H) density plots were used for doublets exclusion; 3) Two-parameter density plots were used to represent the stained population of interest: each axis represented a specific marker/fluorochrome. 4) A quadrant tool was used to generate gates. Negative versus positive populations were selected on the basis of controls ((i) unstained, (ii) stained with primary and secondary antibodies and (iii) only with indicated secondary antibodies).

☒ Tick this box to confirm that a figure exemplifying the gating strategy is provided in the Supplementary Information.